16

Marcasite at the Permian-Triassic Transition: A Potential Indicator of Hydrosphere Acidification

Elena Lounejeva[1], Jeffrey A. Steadman[1], Thomas Rodemann[2], Ross R. Large[1], Leonid Danyushevsky[1], Daniel Mantle[3], Kliti Grice[4], and Thomas J. Algeo[5,6]

ABSTRACT

Abundant pyrite in black shales at the Permian-Triassic Boundary (PTB) from several localities around the world has been regarded as evidence of oceanic anoxia during the end-Permian mass extinction (EPME). However, a significant amount of the "pyrite" in these rocks is not actually pyrite but marcasite, the orthorhombic polymorph of FeS_2. Marcasite is particularly sensitive to changes in pH and fO_2, which theoretically enables it to be utilized as a proxy for geochemical changes in the marine environment. Moreover, its abundance in these PTB rocks suggests that major geochemical changes occurred at this time in the global ocean. In this chapter, we present stable isotope and trace element compositional data for both marcasite and pyrite, which were identified in the stratigraphic interval representing the EPME, along with bulk-rock chemostratigraphic data for the Kockatea Shale, Perth Basin, Australia. We compare marcasite-pyrite intergrowth textures in PTB sedimentary sequences from Meishan D (MD), Opal Creek (OC), Ubara (Ub), and the Kockatea Shale (KS), which represent both shallow continental shelves of the ancient Tethys Ocean (KS, MD) and the abyssal plains of the Panthalassic Ocean (Ub, OC) at the end of the Permian. The textures, trace element geochemistry, and sulphur isotopic analyses of these samples favor a synsedimentary to early diagenetic origin for the sulfides, further supporting the notion that the EPME was at least partially caused by a large-scale pH drop in the global ocean at the PTB. A review of other sedimentary sequences around the globe, including pre- and post-Permian sections, indicates that sedimentary-diagenetic marcasite may be more abundant in the rock record than previously recognized, which carries implications for the geochemistry of the marine environment through geologic time.

16.1. INTRODUCTION

Ocean anoxia and hydrosphere acidification (i.e., acid rain and/or ocean acidification) are likely consequences of a massive release of volatiles in a complex cause-and-effect relationship between the Siberian Traps large igneous province (STLIP) and the end-Permian mass extinction (EPME), as reviewed in recent studies (Bond & Grasby, 2017; Bond & Wignall, 2014; Bryan & Ferrari, 2013; Courtillot & Fluteau, 2014; Ernst, 2014; Ernst & Youbi, 2017; Grice et al., 2005a; Kerr, 1998; Kidder & Worsley, 2010; Kravchinsky, 2012; Nabbefeld et al., 2010; White & Saunders, 2005; Whiteside & Grice, 2016).

[1] *CODES Centre for Ore Deposits and Earth Science, University of Tasmania, Hobart, Tasmania, Australia*

[2] *Central Science Laboratory, University of Tasmania, Hobart, Tasmania, Australia*

[3] *Morgan-Goodall Palaeo, Perth, Western Australia, Australia*

[4] *Western Australian Organic and Isotope Geochemistry Centre, School of Earth and Planetary Science, Curtin University, Perth, Western Australia, Australia*

[5] *Department of Geology, University of Cincinnati, Cincinnati, Ohio, USA*

[6] *State Key Laboratory of Geological Processes and Mineral Resources, and State Key Laboratory of Biogeology and Environmental Geology, China University of Geosciences, Wuhan, China*

Large Igneous Provinces: A Driver of Global Environmental and Biotic Changes, Geophysical Monograph 255, First Edition.
Edited by Richard E. Ernst, Alexander J. Dickson, and Andrey Bekker.

DOI: 10.1002/9781119507444.ch16

Redox analysis in ancient marine sediments commonly makes use of shales and the pyrite present in them. Thus, the presence of organic-rich (black shales) and pyrite-rich shales is suggested to be indicative of an anoxic depositional environment (Dustira et al., 2013; Isozaki, 1997; Rickard, 2012). Furthermore, black shales were proposed to be temporally linked not only to anoxic events and mass extinctions, but also to LIP formation (Meyers, 2014; Zhang et al., 2018). Redox-sensitive trace elements, especially U, V, and Mo, are commonly scavenged from seawater in strongly reducing facies, leading to enrichments in the resulting sedimentary package far above average upper crustal values (Tribovillard et al., 2006).

Acid rain at the end-Permian has been linked to a massive release of volatiles (S, Cl, F) from the Siberian platform sediments during the STLIP formation, and this process may have been an important cause of the contemporaneous terrestrial ecosystem failure and ozone-layer collapse (Black et al., 2013), although the effect of acidification on the extinction of heavily calcifying marine organisms is poorly understood (Doney et al., 2009; Hofmann et al., 2010; Veron, 2008). However, sedimentary proxies for hydrosphere acidification are scarce. Ocean acidification postdating the main pulse of the EPME has been inferred based on geochemical methods developed to evaluate pH variation in palaeo-oceans, such as calcium isotopes in biogenic apatite (Hinojosa et al., 2012; Payne et al., 2010) and boron and lithium isotopic compositions of marine carbonates (Clarkson et al., 2015; Jurikova et al., 2019; Roberts et al., 2018). As these isotopic systems are vulnerable to diagenesis, these proxies require pristine biogenic carbonates, which are rarely available (Hood et al., 2018). Abundant gypsum, a hydrated form of calcium sulphate, was identified along pyrite in Beds 25 and 26 of the Meishan D section. The presence of gypsum in white clay layers lacking carbonates immediately preceding the major mass extinction event in the middle of the Bed 27 was proposed as mineralogical evidence of the end-Permian marine acidification by hydrated sulphuric acid, leading to a pH drop below 3.89 (Liang, 2002). This hypothesis has been widely cited but has not received further support, although stable isotopes of coexisting pyrite and gypsum from cold seeps have provided evidence of variable methane emissions (Lin et al., 2016). Hot acidic Late Permian seas were proposed based on extraordinarily high $^{187}Re/^{188}Os$ ratios and high contents of Re accumulated in P-T successions from the mid-Norwegian shelf and East Greenland (Georgiev et al., 2015).

This study began with LA-ICP-MS analyses of trace element contents in pyrite from the PTB in the Perth Basin as a possible proxy to palaeo-ocean chemistry (Large et al., 2014). A marcasite-containing sample from the Perth Basin was initially discarded from that study due to a presumed late diagenetic origin, but marcasite was not positively identified until a shift in both carbon and sulphur isotopes indicated that this layer was unusual. Assuming the $\delta^{13}C_{org}$ shift is correlative to the EPME, we speculated whether the presence of marcasite at this stratigraphic horizon was a mere coincidence or if it was related to worldwide acid rains due to the STLIP eruptions. We therefore decided to explore further.

Marcasite, as well as pyrrhotite and pyrite, forms in diverse geologic environments under oxic or anaerobic conditions and at varying temperatures, but it is always indicative of a somewhat acidic environment. Marcasite has been reported from many hydrothermal ore deposits (Allen et al., 1912; Newhouse, 1925; Steadman et al., 2016; Thomas et al., 2011) as a result of ascending hot acidic solutions. In the late 1970s, primary marcasite and pyrite were reported forming together at modern seafloor hydrothermal vents and currently forming ore deposits from the Mid-Atlantic Ridge and the East Pacific Rise (Ono et al., 2007; Rouxel et al., 2004). It can form euhedral crystals, swallow-tail twins, colloform or dendritic textures (Grant et al., 2018; Melekestseva et al., 2018; Scott et al., 2009). Experiments simulating hydrothermal conditions confirmed that the rate of marcasite formation is favored by low pH (<5) and established the upper temperature limit for marcasite stability before inversion to pyrite at ~240°C (Murowchick & Barnes, 1986; Schoonen & Barnes, 1991a, 1991b, 1991c; Schoonen, 2004). Following theoretical works (Tossell et al., 1981), Murowchik and Barnes (1986) proposed an experiment-based model, which postulated a deterministic role of H^+ protonation of S_2^{2-} for preferential marcasite formation over pyrite. They argued that the subsequent shift of electron densities distorts the iron coordination around the S-S group, which leads to marcasite formation rather than pyrite.

Early diagenetic marcasite is known from peat and coals formed under slightly acidic conditions (pH 2.1–5.5, measured by Pettijohn, 1957). An unusually high concentration of marcasite has been reported in Holocene clay-peat sediments at Bungawalbin Swamp, NSW, Australia, suggesting that an abundance of marcasite is a valuable environmental proxy for mixed, fresh-brackish swamp environments (Bush et al., 2004).

In cold (2–21°C) methane seeps from the South China Sea, marcasite lamellae were identified in pyrite crystals (Xu, 2010). Marcasite growth was suggested to be a result of pH variation through sorption and anaerobic oxidation of methane molecules on pyrite surfaces, leading to eventual acidification and marcasite precipitation.

Marcasite may also replace pyrite or pyrrhotite (FeS) in hydrothermal, metamorphic, or sedimentary environments, which involves dissolution-precipitation processes. These were simulated by submitting natural pyrrhotite to variable temperatures and pH using different mixtures of inorganic acids and alkaline salts, sulphur and oxygen saturations (Qian et al., 2011). The experiment showed that marcasite is preferentially formed under lower pH and is stable in cold, strongly acidified solutions (pH <3, 21°C).

Late diagenetic marcasite is the most commonly reported form of marcasite in marine sediments. The late diagenetic environment involves cold (5–15°) pore water trapped beneath the sediment-seawater interface (i.e., a closed system) and continual acidification due to oxygen loss and a supply of hydrogen sulfide from microbial sulfate reduction (Berner, 1984).

Early diagenetic marcasite textures in reworked black shales are a potential proxy for multiple episodes of downward oxygenation of bottom waters (Schieber, 2011). The proposed chain of chemical reactions involves oxygen supply oxidizing Fe^{2+} to Fe^{3+}, which, in turn, may oxidize detrital pyrite. The reaction involves H^+ production, but the process is not vigorous, as 14 Fe^{3+} molecules are required to oxidize one FeS_2 molecule. This conclusion precludes fully anoxic conditions during black shale deposition and instead implies an intermittent oxidation of carbonaceous muds through reworking of pyrite debris and subsequent generation of an excess of H^+ required for marcasite formation. .

In short, marcasite formation is favored by and is stable at relatively low pH (0.96–5.5) and temperatures (2–160°C). The processes leading to marcasite formation, however, are poorly constrained.

Here, we present chemostratigraphic results, including C and S isotopes, for the Hovea Member of the Kockatea Shale (Thomas et al., 2004), cored in the Redback-2 oil well in the Perth Basin of Western Australia. We report marcasite-pyrite intergrowths from four different localities associated with the EPME and STLIP. We also compare available data from the different Permian-Triassic (PTB) localities, using $\delta^{13}C$ and $\delta^{34}S$ chemostratigraphy for correlation. These include cherts alternating with shales from Unit II in the Ubara section in central Japan, black shales from Sulphur Mountain Formation in Opal Creek, Canada, and in clays across the PTB Global Stratotype Section and Point (GSSP) in Meishan, China. We use Raman, LA-ICP-MS, and SHRIMP-SI methods for in situ identification and assessment of the geochemical composition of marcasite and pyrite from the Kockatea Shale. We also distinguish positive $\delta^{34}S$ coupled to positive $\Delta^{33}S$ for Mn-rich marcasite opposite that of pyrite in Kockatea Shale. We then review the existing literature on marcasite formation through different geological processes and bring together disparate records about marcasite occurrences (which were reported as pyrite occurrences) at the end-Permian and other younger and older stratigraphic boundaries associated with mass extinctions (and probably with LIP activity). Further, we emphasize that the presence or absence of marcasite in shales has to be determined, as it can substantially influence the interpretation of chemostratigraphic data. Finally, we discuss whether marcasite may indicate eventual hydrosphere acidification linked to LIP activities.

16.2. STUDIED SECTIONS

The present-day location and the depositional setting of the PTB sequences involved in this study are summarized in Table 16.1 and Figure 16.1. The geologic context of the studied sediments is shown in Figure 16.2.

16.2.1. Hovea Member, Basal Kockatea Shale, Western Australia

At the end of the Permian, the Perth Basin was part of a longitudinal rift zone situated between what is now Australia to the east, India to the west, and Antarctica to the south, and facing the open ocean to the north (Cawood & Nemchin, 2001). The paleotectonic and depositional evolution of the basin began as a half-graben breakup of the Precambrian basement of Gondwana in the early Permian and continued through to the Cretaceous (Jones et al., 2011). The Hovea Member is the basal unit (<47 m thick) of the Kockatea Shale Formation (>400 m thick), deposited during Late Permian to Early Triassic subsidence and marine transgression of the Tethys Ocean into the Perth Basin. The Permian-Triassic transition within the Hovea Member is associated with an upward change from inertinitic (charcoal-rich, organic-poor) to sapropelic (oil prone, organic-rich) rock types (Redback-2 and Hovea-3 completion reports). The conodont *Hindeodus parvus,* a diagnostic indicator of the basal Triassic, is absent from the Hovea Member, but the presence of synchronous sharp shifts in C and S isotopes suggests a short-lived hiatus between the inertinitic and sapropelic intervals of the sequence (Grice et al., 2005a, 2005b, 2007; Grotheer et al., 2017). A rapid shallowing at the end of the Permian followed by a rapid deepening in the Early Triassic was inferred based on a short-lived decrease, followed by a rapid increase in the gamma ray log response in the Hovea Member lithofacies defined in the Redback-2 well (Jafary Dargahi, 2014). Therefore, the deep-water Late Permian pyritic mudstones and black shales are separated from the shallower

Table 16.1 Present-Day Location of the Sedimentary Sequences Involved in This Study

Locality name	Coordinates	Source
Redback-2 well, WA	29.457595S, 115.16166E	Redback-2 Completion Report, Origin LTD
Hovea-3 well, WA	29.319213S, 115.03972E	Hovea-3 Completion Report, Origin LTD
Meishan, Zhejiang province, China	31N, 119.11667E	Yin et al., 2005
Ubara, Ayabe area, Kyoto Prefecture, Japan	35.189896N, 135.2515E	Algeo et al., 2011
Opal Greek, Alberta, Canada	50.90933N, 29.319213W	Schoepfer et al., 2013

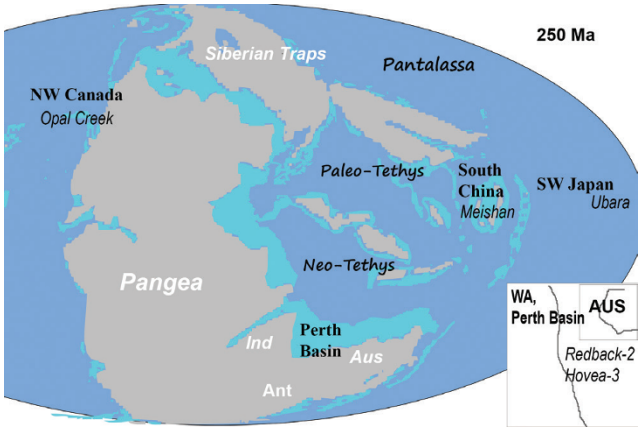

Figure 16.1 Palaeogeographic locations of the PTB sequences in this study, consistent with recent paleotectonic reconstructions (modified from Blakey & Ranney, 2018).

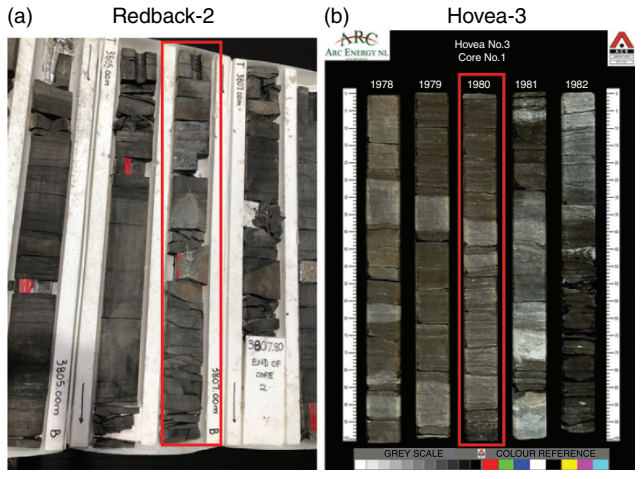

Figure. 16.2 Representative photos of Permian-Triassic boundary sequences studied in this paper. (a) Redback-2 drill core, 3,805–3,807 m depth interval; (b)Hovea-3 drill core, 1,978–1,982 m depth interval.

Early Triassic fossiliferous mudstones by finely interbedded calcareous, siliceous, and carbonaceous mudstones, which represent the Permian-Triassic Boundary (Jafary Dargahi, 2014). The marine transgression coincided with regional volcanic and intrusive magmatic activity (Gorter & Deighton, 2002; Gorter et al., 2009; Veevers & Tewari, 1995) and a marked change toward extrabasinal sourcing of detrital material, as recorded by detrital zircons in Lower Triassic sandstones (Cawood & Nemchin, 2000). Based on a study of biomarkers in the Hovea-3 core and GSSP Meishan sediments, Grice et al. (2005a) suggested the development of photic-zone euxinia during the Early Triassic in Western Australia and China, thus pointing to a sulfidic driver for mass extinction. Summarizing the above, the Permian-Triassic transition within the Perth Basin has coincided with sea level variation, active regional magmatism, and a change in the provenance of detrital zircons, all suggesting an active tectonic setting at that time.

For this study, we sampled the Hovea Member mudstones from two drill holes, Hovea-3 (H3; 42 samples from 1,968–1,993 m depth interval) and Redback-2 (RB2; 42 samples from 3,788–3,836 m depth interval), both of which are stored at the Geological Survey of Western Australia's core library in Perth, WA. Samples were generally 10–15 cm of quartered drill core, taken every 1–2 meters. For petrographic, trace element, and Raman spectroscopic work, a thin (~5 mm) disc of material ~25 mm in diameter was cored out of selected samples and placed in a mount of epoxy resin. Once the resin cured, the exposed surface of the mount was polished to 1 μm finish.

16.2.2. Lower Yinkeng Formation, Meishan, China

The Meishan section, deposited in a shallow Tethyan environment, has been extensively studied as the GSSP for the PTB (Grice et al., 2005a; Jin et al., 2006; Yin et al., 2005). The PTB at Meishan is defined by the first appearance datum of the conodont, *Hindeodus parvus*, in Bed 27c-d of the lower Yinkeng Formation (Shen et al., 2011). The most recent timeline for mass extinction (Burgess et al., 2014) places the main pulse of mass extinction between 251.941 ± 0.037 Ma and 251.880 ± 0.031 Ma, based on U-Pb dating of zircons from intercalated volcanic rocks in Beds 25 and 28, respectively. This timeline restricts the extinction to a relatively short interval of a few tens of thousands of years in the middle of the one-million-year-long STLIP activity (252.3–251.3 Ma, Burgess & Bowring, 2015, Burgess et al., 2014). The extinction interval is immediately preceded by a negative $\delta^{13}C$ excursion in Bed 24e, which is thought to have a temporal and genetic link to the second stage of STLIP formation distinguished by massive sill intrusions into

Siberian Craton sedimentary rocks and a consequent release of greenhouse gases (Burgess et al., 2017). Based on a detailed review of biotic and sedimentary records of the PTB from the Meishan section, Chen and coauthors (2015) linked the initial pulse of the biological crisis at the base of Bed 25 to a rapid increase in the sea-surface temperatures by 9°C and a period of short anoxia or acidification. Framboidal and euhedral pyrite (but not marcasite) have been described throughout the section.

Grey clayish limestones from Beds 24c, d, e, 27ab-cd, 29ab, 30m, 31, 33, and 45 from the lower Yinkeng Formation in the Meishan D section were sampled in this study. The samples were placed in epoxy resin to preserve the original texture and polished, exposing about 2 cm^2 for analysis.

16.2.3. Abyssal Black Shales, Ubara, Japan

The Ubara section outcrop, located in the Ayabe area, Kyoto Prefecture, Japan, represents deep waters of the Panthalassic Ocean during the Late Permian. Algeo et al. (2011) suggested that the transition from the Latest Permian grey organic-poor cherts (Unit II) to the Triassic black shales (Unit III) was accompanied by increased primary productivity, euxinia within the oxygen-minimum zone (OMZ), and decimation of the radiolarian zooplankton. The Triassic age is established based on the occurrence of *H. parvus* in the lower part of the black shales (Yamakita et al., 1999) and the location of the PTB was placed at the base of Unit III. Pyrite is ubiquitous in both Units (2%–10%) and is predominantly present as very fine-grained framboidal pyrite. A 2 cm-thick pyrite layer is present 10 cm below the suggested PTB. The S-isotopic composition of pyrite is slightly heavier in the cherts through one meter below the pyrite layer ($\delta^{34}S_{py}$ varies from −21.9 to −30.5‰, average −27.4 ± 2.7‰, n = 14), but changes to lighter in the pyrite layer and in the black shales above (from −25.1 to −36.8‰, average −31.3 ± 5.5‰, n = 11).

This study examined 15 samples spaced by 5–6 cm from a 1.3 m section below the PTB, including cherts, the pyrite layer and the black shales. The samples were placed in epoxy resin to preserve the original texture and polished, exposing about 2 cm^2 for analysis.

16.2.4. Sulphur Mountain Formation, Opal Creek, Kananaskis Valley, Canada

The Opal Creek section is an outcrop of the Sulphur Mountain Formation (SMF) inferred to be deposited on an outer shelf in deep waters of the Panthalassic Ocean. The SMF starts with a transgressive package exposing a conformable contact between 0.5 m of bioturbated siltstone and 2 m of black shales (Schoepfer et al., 2013, their Figure 4). The stratigraphic PTB boundary was constrained by the first occurrence of *H. parvus* in the middle of black shales, ~1 m above the contact between siltstones and black shales. A few centimeters below this contact, a thin layer of the late Permian extinction interval, dated at 251.95 Ma (Shen at al., 2011), was identified by the absence of siliceous sponges from bioturbated siltstones. An episode of euxinia about 30 cm below the contact was suggested based on the presence of a 1 cm thick pyrite layer in bioturbated siltstone, and an extension of low dissolved oxygen up to the contact with pyritic black shale was based on an observed increase of U, Mo, and V contents in the rocks (Schoepfer et al., 2013). The pyrite layer is distinguished by a positive spike of $\delta^{13}C_{org}$, drop of $\delta^{15}N$ (Schoepfer et al., 2012) and heavier $\delta^{34}S_{py}$ (Schoepfer et al., 2013), interpreted as a cessation of highly productive coastal upwelling where vigorous denitrification and sulfate reduction occurred at a midwater oxygen minimum. Massive marcasite intergrown with pyrite was identified in this layer, although the authors interpreted its presence as the product of a cryptic hydrothermal event (Schoepfer et al., 2013). The age of the pyrite-marcasite layer is not older than 252 Ma, assuming it is correlative to the transgression seen elsewhere (Shen et al., 2019), and is consistent with biostratigraphy (Schoepfer et al., 2013).

This study examined the massive pyrite layer sample and six samples (about 10 cm^3 each) from 2 m of pyritic shales above the mass extinction interval. The samples were prepared in the manner as above, that is, mounted in epoxy and polished.

16.3. METHODS

Marcasite and pyrite were first recognized under reflected light and discriminated by the micro-Raman technique using Renishaw inVia Raman microscope with a Streamline instrument at the Central Science Laboratory, University of Tasmania. Sulfide crystals were found on the polished surface and analyzed using 50 times, 1800 l/mm grating, step size of 0.5 × 0.5 μm and an excitation laser of 532 nm with exposure time of 30 s and laser power of 0.5 mW in the interval between 250 and 500 cm-1. Spectral acquisition, curve fitting, and baseline correction were conducted using WiRE 4.2 software. The spectra were compared against the RRUFF database.

The whole-rock fine powder was treated with 3M HCl for 6 h to destroy carbonates and rinsed with distilled water until neutrality. Total organic carbon and sulphur were then analyzed on ELTRA CS-2000 elemental analyzer using AR4007 and AR4015 Alpha Resources standards for external calibration. Isotopic ratios of carbon and sulphur were also performed on carbonate-free

whole-rock fraction using an Isoprime EA-IRMS instrument, yielding an uncertainty of ±0.03‰ assessed on USGS-40, -24, -41, and NBS-21 calibration standards and RSD = 2.5% between the standards replicates.

In situ measurements of ^{32}S, ^{33}S, and ^{34}S were conducted using the Sensitive High-Resolution Ion Microprobe for Stable Isotopes (SHRIMP-SI) at the Research School of Earth Sciences, Australian National University (ANU) (Ireland et al., 2008). Samples were placed in composite mount together with reference materials, polished, coated with gold, and degassed overnight before entry into the SHRIMP-SI sample chamber. The average of $\delta^{34}S$ measured on reference material, Ruttan and Balmat pyrites was +1.1 ± 0.2‰ and +14.4 ± 0.3‰, respectively, in a good agreement with previously published data (+1.408 and +16.12 ‰; Cabral et al., 2013).

Whole-rock (WR) chemical composition was assessed through ME61 ALS Minerals method (four acids digestion followed by ICP-OES and ICPMS analysis) achieving an analytical precision within target range on duplicates and reference materials GBM908-10, MRGeo-08, GEOMS-03, and OGGeo-08.

The trace element contents in the studied minerals were analyzed by laser ablation-inductively coupled-mass spectrometry (LA-ICP-MS) at CODES, University of Tasmania. The instrument combines a RESOlution 193 nm excimer laser, coupled to an Agilent 7700x ICP-MS. For the trace element map, signal was acquired in time-resolved mode using laser beam of 5 μm, laser fluence of ~3.5 J/cm^2, and a repetition rate of 5 Hz. The signal from carrier gas with no ablation was regularly acquired to correct for instrumental background. The following reference materials were used for primary calibration and assessment of elemental contents: STDGL2b2 (Danyushevsky et al., 2011) and STDGL3 (Belousov, 2014; Belousov et al., 2015) for siderophile and chalcophile elements; GSD-1G (Jochum, 2014) for lithophile elements; and PPP-1 pyrite for sulphur (Gilbert et al., 2014).

Twenty-nine of the studied samples were described by Morgan-Goodall Palaeo, Perth, Western Australia, using standard palynological processing methods (Phipps & Playford, 1984; Traverse, 2007). The crushed samples were subject to acid dissolution, with HCl and HF used to digest the carbonates and silicates, respectively. Heavy liquid separation using $ZnBr_2$ removed the remaining mineral matter and finally some samples were oxidized using HNO_3 to remove fine organic clumps and to lighten the palynomorphs. As most samples yielded only low abundances of poorly preserved palynomorphs and some were devoid or near-devoid of organic-walled microfossils, the palynological study from other nine core samples from Redback-2 was also considered to complete this study (Redback-2 Completion Report, 2010).

16.4. RESULTS

Chemostratigraphic data for the Kockatea Shale samples from Redback-2, including whole-rock geochemistry, carbon and sulphur isotopes, are present in Table 16.2, along with the palynological zones as defined in this study. Representative petrographic features of pyrite and marcasite from all the studied samples are presented in Figure 16.3. Raman and LA-ICP-MS element distribution maps in pyrite and marcasite are shown in Figure 16.4. Data for sulphur isotopes analyzed in situ on marcasite and pyrite are presented in Table 16.3 and Figure 16.5.

16.4.1. Palynology

Palynological analysis of Redback-2 mudstones of the Kockatea Shale reveals definitive Permian palynofloras in the bioturbated carbonaceous shales from 3,835.30 to 3,808.90 m. These *Dulhuntyispora parvithola* Zone assemblages are dominated by terrestrial spores and pollen, including diagnostic Permian taxa such as *Didecitriletes ericianus, Dulhuntyispora parvithola, Microbaculispora trisina, Praecolpatites sinuosus,* and *Pseudoreticulatispora pseudoreticulata*. The inertinitic interval in Redback-2 is recognized by abundant black (burnt?) wood, which continues further up to 3,806.15 m. This inertinite-rich interval is widely recognized across the Perth Basin (Jones et al., 2011) and provides evidence for wide-ranging wildfires around the basin. Evidence for extensive wildfires are consistent with atmospheric oxygen levels of at least 15% during the latest Permian (Glasspool & Scott, 2010).

Triassic assemblages dominated by spiny acritarchs (*Micrhystridium* spp. and *Veryhachium* spp.) were found in the overlying 14 m of laminated fossiliferous mudstones from 3,788.7 m to 3,803.2 m. These assemblages and the increased abundance of sapropelic organic material are diagnostic of the earliest Triassic marine incursion that is also widely reported from the *Krauselisporites saeptatus* Zone across the Perth Basin (Shi et al., 2010).

Samples from the interval between 3,804 m and 3,808.9 m are either barren or contain very sparse, poorly preserved spore-pollen assemblages that are indeterminate. The latest Permian age (Changhsingian) for this interval is suggested by *Revitriletes hennellyi* found at 3,806.51 m (this study) and *Protohaploxypinus microcorpus* Zone at 3,804.14 m (Redback-2 Completion Report). However, the early Triassic foraminifer *Paleomayncina termieri* was reported at 3,805.92 m (Jafary Dargahi, 2014, Figure 3.5f), more than a meter deeper than the last appearance of the Late Permian palynofacies. This suggests a possibility of postdepositional sediment reworking.

Table 16.2 Palynological Zones and Chemostratigraphic Data for the Kockatea Shale, Hovea Member Mudstones From the Redback-2 Drill Well

	Lythology	Depth	TOC	Fe	S	Mn	Fe	Mo	Cu	U	U/Re	$d^{34}S$	$d^{13}C_{org}$
	*	(m)	wt%	wt%	wt%	/Al	/Al	/Al	/Al	ppm		‰	‰
Early Triassic, *K. saeptatus*	F	3,788.7	2.5	5.2	4.3	162	0.5	0.9	17	3.1	443	–21.55	–30.62
	F	3,790.0	6.5	8.0	8.2	326	1.0	1.9	14	4.2	350		
	F	3,791.7	4.8	10.4	11.6	54	1.4	4.5	15	3.4	179	–28.34	–29.37
	F	3,796.8	7.0	11.3	13.3	69	1.8	10.0	17	5.7	259	–25.95	–24.43
	F	3,797.8	5.5	8.4	8.8	139	1.4	2.9	17	4.6	354		
	F	3,798.6		14.9		72	2.3	5.5	15	3.0	273	–20.93	–28.61
	BS	3,799.2	3.9	6.0	6.4	44	1.1	2.7	14	2.6	236	–28.08	–29.40
	F	3,799.9		4.2		361	0.5	0.2	15	2.8	560	–21.10	–20.45
	F	3,800.4		8.6		229	1.0	1.7	20	4.5	409	–25.70	–30.61
	F	3,800.6	2.5	10.8	11.6	68	1.3	2.5	16	3.9	244	–15.55	–24.41
	F	3,801.1	5.1	6.8	6.7	73	0.7	1.7	20	4.1	410	–25.65	–29.87
	F	3,801.7	5.9	5.2	5.2	255	0.7	1.2	21	3.2	291	–26.69	–27.44
	F	3,802.1	4.8	11.9	14.0	175	1.3	1.8	15	3.8	380	–25.97	–30.79
	F	3,803.2	4.5	4.2	3.9	813	0.6	0.3	14	3.6	514	–26.84	–31.07
	F	3,803.2		6.8	3.9	44	0.7	1.7	23	5.0	500	–26.84	–31.07
	F	3,804.6	3.9	8.8	8.9	66	1.0	4.5	17	6.0	250	–32.05	–31.64
Indeterminate	C	3,805.4	4.1	7.2	6.5	30	0.7	2.1	15	6.4	376	–35.44	–30.96
	BS	3,806.2	0.7	3.7	0.9	30	0.4	0.3	5	6.3	394	–42.24	–31.31
	BS	3,806.5	1.9	3.3	1.3	25	0.3	0.1	7	4.6	1,533	–39.64	–32.34
	F,S,BS	3,806.6	0.7	6.2	4.7	45	0.9	0.2	7	1.8	360	11.48	–27.51
	S–C	3,807.4	2.1	3.9	0.7	45	0.4	0.2	5	15.2	171	–49.87	–24.86
	F	3,808.1	1.5	3.9	0.2	49	0.5	0.2	5	7.4	247	–45.08	–24.78
Late Permian, *D. parvitola*	C	3,808.9	2.2	2.9	0.5	34	0.4	0.1	5	3.7	142	–28.93	–25.22
	P	3,809.6	2.5	2.9	0.7	33	0.4	0.1	7	3.5	175	–44.59	–25.09
	P	3,809.7	1.2	3.7	0.8	47	0.4	0.2	5	3.3	300	–52.18	–24.55
	P	3,810.4		4.0		22	0.5	0.2	7	3.1	207	–49.61	–24.61
	BS	3,811.8	2.6	5.2	3.5	28	0.7	1.6	8	3.4	126	–51.42	–25.26
	BS	3,812.2	1.4	3.4	0.7	28	0.5	0.2	7	3.2	80	–52.57	–24.44
	BS	3,812.7	1.1	3.6	0.2	40	0.5	0.1	7	3.1	182	–29.06	–24.07
	BS	3,814.5		3.2		30	0.5	0.2	7	3.3	220	–39.95	–25.33
	BS	3,816.0	2.2	4.1	1.1	18	0.5	0.3	5	3.3	157	–54.54	–24.51
	BS	3,816.9	2.7	4.6	2.3	14	0.5	0.6	6	3.7	148	–51.50	–25.46
	BS	3,818.1	2.1	3.5	0.6	16	0.5	0.2	7	2.8	147	–45.88	–25.00
	BS	3,821.3	1.4	3.2	0.5	20	0.5	0.3	8	2.6	186	–35.62	–25.32
	BS	3,821.5	1.4	3.1	0.3	14	0.5	0.2	5	2.4	141		
	BS	3,823.8	3.2	4.6	2.2	14	0.6	0.4	5	2.8	147		
	P	3,827.4	2.7	4.6	2.4	11	0.6	0.3	6	2.5	147	–41.66	–23.90
	P	3,830.6	3.1	2.8	0.7	8	0.3	0.1	5	3.1	282	–41.04	–25.36
	P	3,831.2	3.2	3.6	1.3	11	0.5	0.2	4	2.5	156		
	S–C	3,832.1	2.8	3.5	1.1	12	0.4	0.1	3	2.6	200	–46.86	–23.16
	S–C	3,834.3		5.2		21	0.9	2.2	7	2.4	120		
	C	3,835.3	2.1	3.1	1.5	10	0.4	0.2	3	2.8	127		

*F = fossiliferous, S = siliceous, P = pyritic, C= calcareous mudstones, BS = black shales, as defined by Jafary Dargahi (2014).

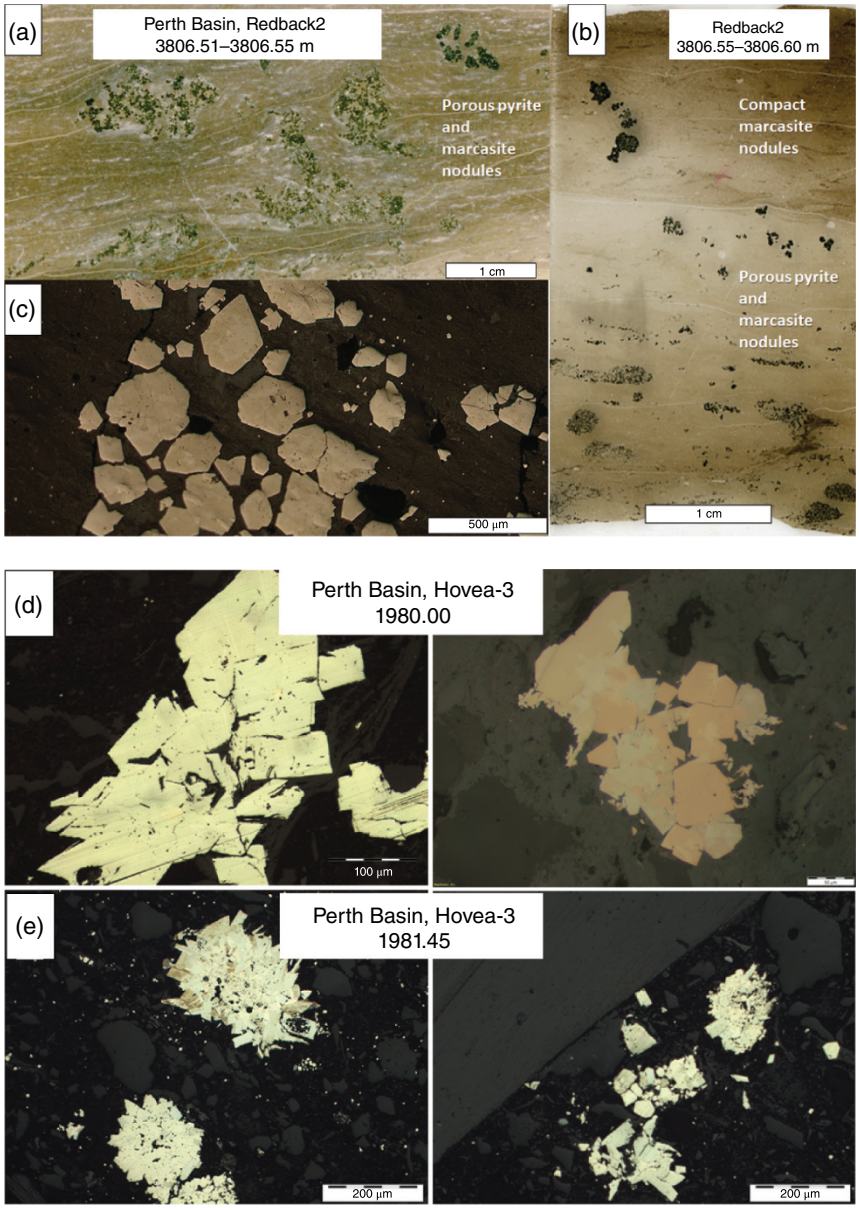

Figure 16.3 Petrographic features of marcasite and pyrite from PTB horizons. **Iron bisulfides in Kockatea Shale**. (a) RB2: 3,806.51–3,806.51 m, scanned image of polished thin section. Note differential compaction around sulfide nodules, which are mainly composed of euhedral marcasite associated with early diagenetic silica (whitish color). (b) RB2: 3,806.55–3,806.60 m, scanned image of polished thin section. (c) RB2: 3,806.55, euhedral crystals of marcasite and pyrite**.** (d) H3: 1,980.00 m, well-developed marcasite blades in crystalline aggregate; (e) H3: 1,981.45 m, intergrowth of marcasite and pyrite. Note also clastic particles and tiny angular iron sulfides disseminated in the sediment; (f–k) H3: 1,982.30 m. (f) Marcasite-pyrite microcrystalline nodule in thin section. Note differential compaction of siliciclastic material around pyrite-marcasite nodule. (g–k) Details of the same nodule at higher magnification. Note both marcasite (m) and pyrite (p) were formed in porous spaces as well as in microcrystalline aggregates, as revealed by Raman spectroscopy. **Iron bisulfides in Meishan section**. (l, m) MD-27ab top and bottom. Marcasite (bluish) core overgrown by euhedral pyrite rim. (n, o) MD-30 clay. Marcasite (bluish) core overgrown by euhedral pyrite rim. (p, q) MD-49 clay. Sulfide nodules (up to 1 mm) with marcasite rims and close-up of one of the crystals. **Iron bisulfides in Ubara section Unit II**. (r) Ub-18, Chert 12 cm above the massive pyrite layer, i.e., very close to the suggested PTB. This photo is a typical appearance of sulfides in Unit II cherts, i.e., rare chains of euhedral crystals along stratification. Close-up of marcasite (bluish) domains weakly distinguishable from pyritic core, both enclosed in coarse euhedral crystals of later pyrite. (s) Ub-16 Chert sample with a thin bed of shales. The sample comes from a layer 1 cm below the massive pyrite layer and about 12 cm below the suggested PTB. Euhedral pyrite overgrown by anhedral crystals. Close-up of anhedral crystals composed of pyrite and marcasite domains in the core and outer rims formed by fine radial pyrite. This texture suggests pH fluctuation or nucleation rate variation in this microenvironment resulting in a finely banded pattern. **Iron bisulfides in Opal Creek section**. (t) Marcasite in black shale 30 above the EPME interval. Radiating pyramidal and isometric crystals of marcasite form an intermediate rim between porous pyrite core and a thinner rim of well-crystallized pyrite crystals. (u) A framboidal aggregate of bisulfides from black shale 90 cm above the EPME and close to the PTB. The aggregate is composed of porous and recrystallized pyrite and marcasite filling space between framboids and completing the surrounding rim. Photomicrographs (h)–(k), (m), (o)–(q) were taken under reflected light during Raman spectra analytical sections.

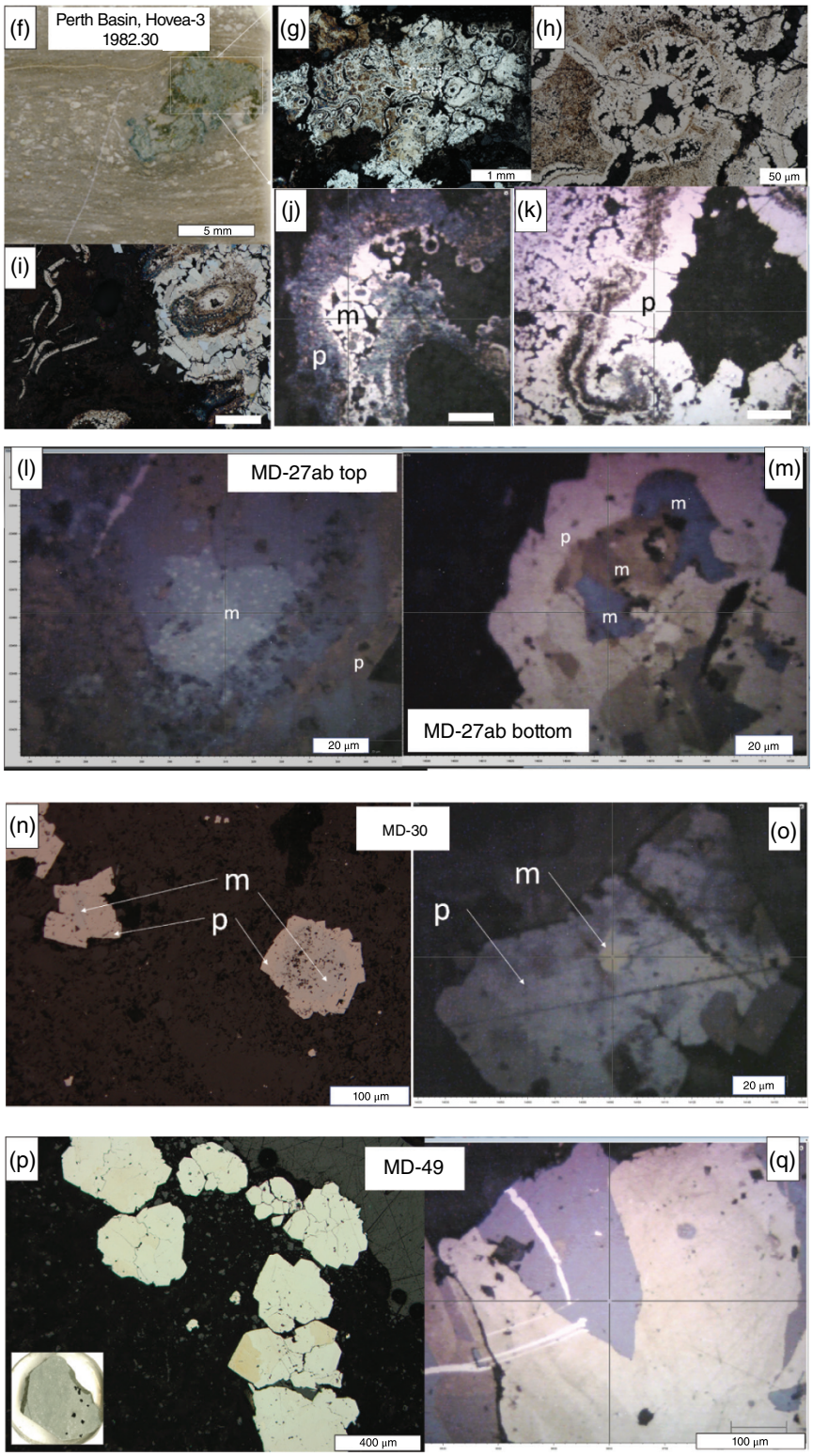

Figure 16.3 (Continued)

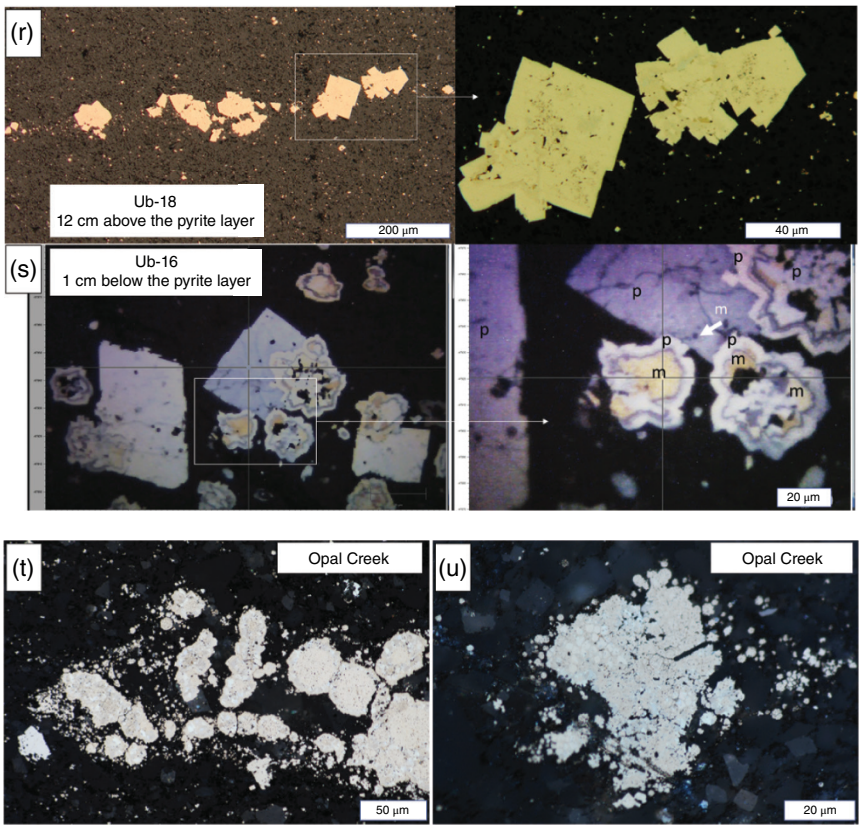

Figure 16.3 (Continued)

Table 16.3 Summary for Sulfur Isotope Data in the Studied Samples and in Ruttan and Balmat Standards

Sample	Calculated	$d^{33}S_{VCDT}$	± (1s)	$d^{34}S_{VCDT}$	± (1s)	$D^{33}S$	± (1s)
RB2_3806.55m_mrc		1.46	0.05	2.70	0.04	0.06	0.04
RB2_3806.55m_mrc		6.07	0.07	11.86	0.41	–0.04	0.07
RB2_3806.55m_mrc		8.91	0.04	17.35	0.23	0.01	0.04
RB2_3806.55m_mrc-py_?		–6.18	0.04	–12.15	0.07	0.09	0.05
RB2_3806.55m_py		–6.43	0.09	–12.70	0.10	0.12	0.09
RB2_3806.55m_py		–6.96	0.03	–13.56	0.10	0.03	0.03
RB2_3806.55m_py		–7.06	0.10	–13.66	0.11	–0.01	0.09
RB2_3806.55m_py		–6.89	0.07	–13.05	0.08	–0.16	0.08
Opal Creek_py		–17.73	0.04	–34.18	0.07	0.01	0.04
Opal Creek_py		–18.32	0.04	–35.44	0.06	0.08	0.04
Opal Creek_py		–18.76	0.06	–36.36	0.11	0.13	0.05
Opal Creek_py		–17.73	0.02	–34.28	0.07	0.07	0.02
Opal Creek_py		–19.60	0.03	–37.69	0.11	–0.02	0.03
Opal Creek_py		–18.87	0.03	–36.62	0.10	0.15	0.03
Opal Creek_py		–15.37	0.03	–29.72	0.09	0.04	0.04
Opal Creek_py		–14.96	0.04	–29.02	0.08	0.08	0.04
Ruttan	mean	0.60	0.05	1.11	0.08	0.03	0.05
Ruttan	stdev	0.20		0.20		0.20	
Balmat	mean	7.41	0.05	14.40	0.08	0.02	0.05
Balmat	stdev	0.05		0.27		0.12	

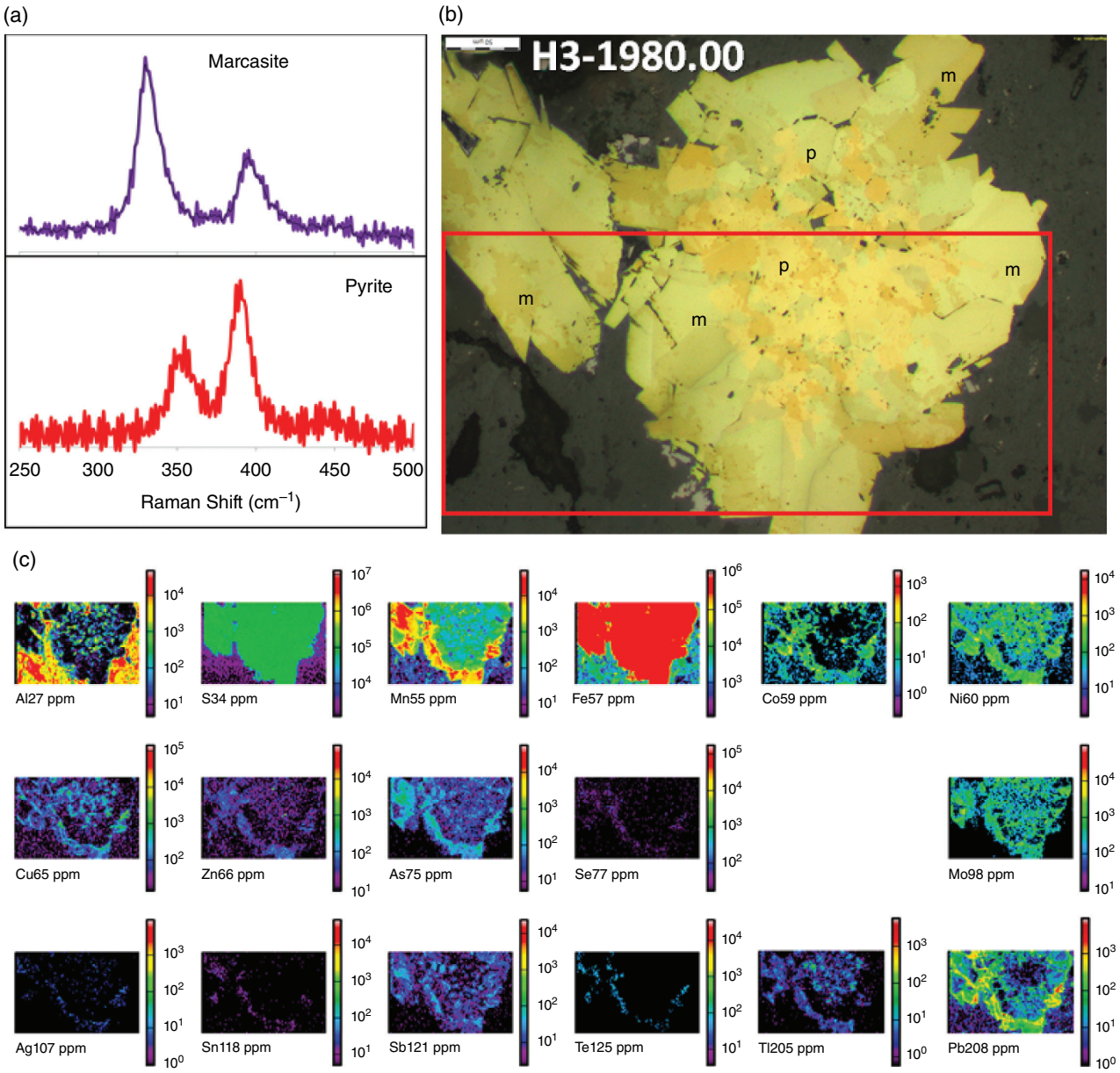

Figure 16.4 Petrography of marcasite and pyrite from Permian-Triassic sequences. (a)–(c) Iron bisulfides from the Kockatea Shale, Hovea-3, 1,980.00 m depth. (a) Representative Raman spectra for marcasite and pyrite. (b) Reflected light, enhanced contrast, scale bar 50 µm. Pyrite, a likely precursor, was identified by Raman only inside the lightest yellow anhedral patches in the center of the crystal. Note four different colors, protruding relief, and lack of sharp boundaries between the two phases. The red rectangle marks the area selected for Raman and LA-ICP-MS imaging. (c) LA-ICP-MS maps of distribution of trace elements contents; ppm = parts per million; scale bars are logarithmic. Note high concentration of Mn (>1,000 ppm) together with higher Pb, Zn, and As preferentially concentrated in marcasite, forming a geochemical rim, which is not petrographically distinguishable. (d)–(g) Iron bisulfides from the Kockatea Shale, Redback-2, 3,806.55 m depth. (d) Reflected light, enhanced contrast, scale bar 50 µm. Note at least three different colors and internal relief of the euhedral crystals. Marcasite structure for the entire crystal was confirmed by Raman spectroscopy. Red squares mark the areas selected for LA-ICP-MS and Raman imaging. (e) The map shows that the difference in the peaks position does not exceed 2.5 cm^{-1} (color scale bar) indicating a homogeneous composition. The change of color reflects slight variations in crystal orientation. (f) The map showing that the peak position varies between 323 and 325 cm^{-1} (green-purple color on the scale bar). The position can be shifted up to 327 cm^{-1}, seen as yellow and mint green straight lines, likely on the fronts of crystal growth. (g) LA-ICP-MS maps of trace elements content and distribution in the same crystals; ppm = parts per million (microgram/gram); scale bars adjusted for element concentration. Note: (1) a high concentration of Mn (> 1,000 ppm) on marcasite edges and "hourglass" shape domains, likely due to crystallographic control; (2) elevated As, Sb, and Mo are also confined to marcasite; (3) Co, Ni, and especially Pb and Bi, are low in marcasite but outline the aggregate boundaries suggesting adsorption.

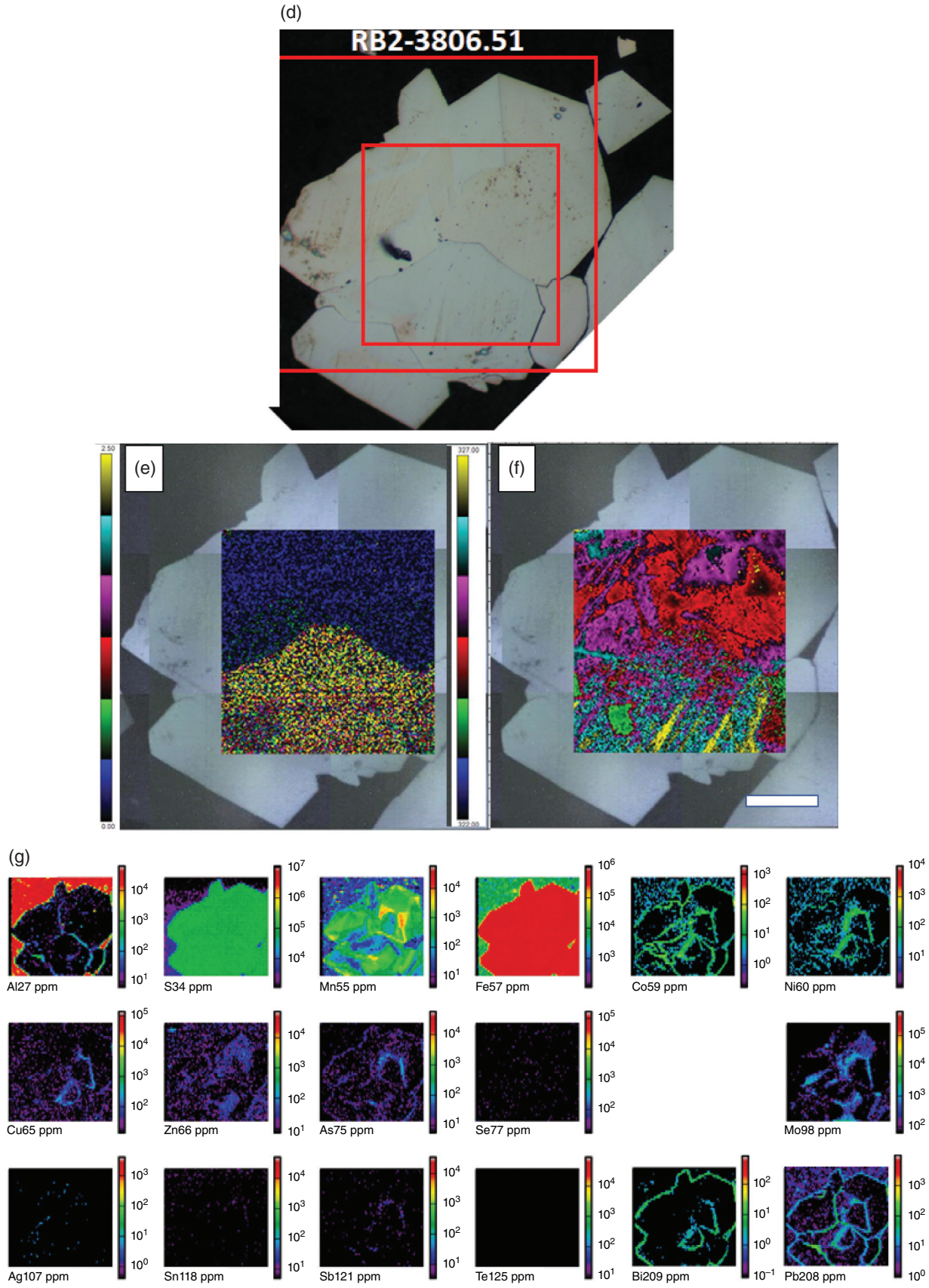

Figure 16.4 (Continued)

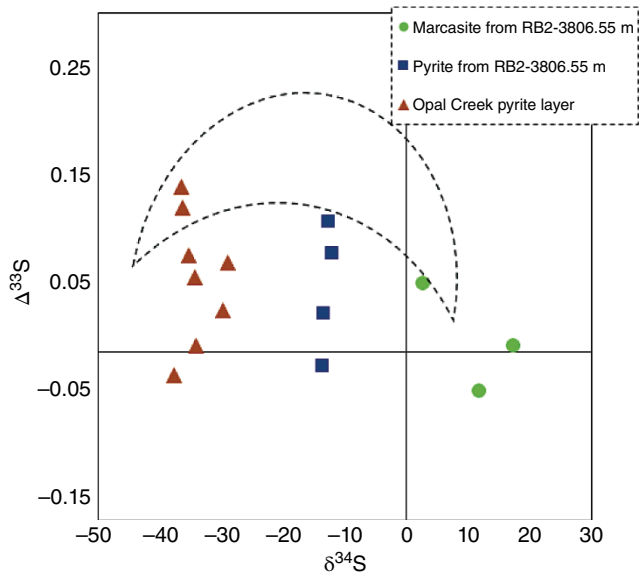

Figure 16.5 Summary of $\Delta^{33}S$ vs. $\delta^{34}S$ for sedimentary pyrite in Redback-2 and Opal Creek performed in this study via SHRIMP. The black dashed shape roughly outlines the area where quantitative sulphate reduction is expected (Tostevin et al., 2014) but sulphur disproportionation may occur (Zhang et al., 2017). Note a distinctive signature of marcasite with positive $\delta^{34}S$ coupled to negative or positive $\Delta^{33}S$.

In the Hovea-3 drill hole, the PTB was previously defined between 1,980.85 m and 1,981 m based on palynology (first appearance of the Triassic bivalve *Claraia* and a negative excursion of $\delta^{13}C$; Hovea-3 Completion Report, 2003; Thomas et al., 2004), which correlates with the presence of C_{33} alkylcylcohexane and other unique biomarkers (Grice et al., 2005a; Spaak et al., 2018).

16.4.2. Petrography of Pyrite and Marcasite

Marcasite identification under reflected light was done based on strong pleochroism, protruding relief, a pale bluish tint, and fast oxidation in air. Optical identification can fail though as revealed by posterior micro-Raman analysis. The most typical aspects of pyrite-marcasite intergrowth from the studied sediments are shown and described in Figure 16.3.

Perth Basin, Kockatea Shale, Hovea Member

Pyrite is present throughout the Hovea Member in all sedimentary facies, as framboids, nodules and veins. The size of pyrite framboids was estimated for four samples from Redback-2 as a weighted average from back-scattered electron images. Framboids from the deeper sediments at 3,831 m are larger (30 ± 3 μm) than those at 3,810 and 3,808 m (9 ± 6 μm), declining to 8 ± 1 μm at 3,805.4 and 6 ± 4 μm at 3,804.6 m. These latter framboids are small enough to have formed in the water column before settling into the mud on the seafloor.

Marcasite in Hovea Member occurs in both drill holes, Hovea-3 and Redback-2, within the P-T transitional intervals, that is 1,980.00–1,982.3 m and 3,806.51–3,806.55 m, respectively. A variety of marcasite crystal shapes have been observed in the transitional P-T interval in the Hovea Member, including small (10–30 μm) angular disseminated crystals, large clusters of euhedral blades, isometric orthorhombic crystals up to 500 μm across, and microcrystalline aggregates (Fig. 16.3d–k). Crystalline marcasite-pyrite aggregates are up to 500 μm in diameter, whereas disseminated angular crystals are much smaller (6 ± 1 μm) similar in size to pyrite framboids. A large (>15 cm diameter) elliptical siderite nodule is present just above the interval where marcasite was also identified (Fig. 16.2). The relationship of marcasite to pyrite changes upward within the sequence. In the deeper layer where the first occurrence of marcasite has been detected, alternating layers of pyrite and marcasite microcrystals in an oscillatory or banded texture form porous nodules (H3: 1,982.3 m, Fig. 16.3f–k). Patchy or acicular intergrowths of both sulfides occur in the layer one meter up (H3: 1,981.45, Fig. 16.3e). Euhedral crystals of marcasite with remnants of pyrite in the core are characteristic for polycrystalline aggregates 0.5 mm large in the overlaying sediments (RB2: 3,806.51–3,806.55; H3: 1,980m; Fig. 16.3a–d). This latter interval is where the last marcasite occurrence has been observed and it is the same interval where a shift in $\delta^{13}C_{org}$ values occurs, as described below.

Meishan D Section

In the Meishan D section, marcasite was identified in the Lower Triassic clays within Beds 49, 31, and 30, but also in Bed 27 (in both Permian MD-27ab and Triassic MD-27cd), a few centimeters above Bed 24e associated with the EPME. In the Meishan clays, the textural relationship between iron bisulfides also changes upward within the sequence. In the MD Bed 27, anhedral marcasite cores surrounded by euhedral pyrite suggest marcasite was the likely precursor for pyrite (Fig. 16.3l,m); the same relationship is also present in the upper clay of MD-30, but there the pyrite rim is thicker (Fig. 16.3n,o). Nevertheless, in clay from MD-49 layer, which is a few meters above the PTB, marcasite is the main phase in sulfide nodules up to 0.6 mm in diameter, randomly distributed in the surrounding clay with no evidence of sulfide-silicate matrix interaction (Fig. 16.3p,q).

Ubara Section

In the Ubara section, marcasite was identified in cherts and in black shales below the PTB (Unit II). Variable

textures and relationships between marcasite and pyrite were observed in chains of fine crystals of pyrite and marcasite, aligned along bedding planes and as disseminated crystals (Fig. 16.3r,s).

Opal Creek, SMF, Section

In Opal Creek, marcasite was identified along pyrite in two samples within one meter of black shales between the Latest Permian Mass Extinction (LPME) and the PTB, as those were previously defined. In the sample 30 cm above the mass extinction layer, marcasite forms a crown around porous pyrite cores, which, in turn, is surrounded by a thin rim of nonporous euhedral pyrite crystals. In the sample 90 cm above the mass extinction and therefore very close to the PTB, marcasite is more abundant and occurs either in mixed sulfides, framboids, euhedral crystals, or polycrystalline aggregates. In both samples, marcasite-pyrite intergrowth still preserves the texture of framboidal aggregates (Fig. 16.3t,u).

16.4.3. LA-ICP-MS and Raman Analysis

Identification of marcasite in the above samples was further confirmed by micro-Raman analysis. The main Raman shifts are at 344 and 380 cm^{-1} for pyrite versus 324 and 386 cm^{-1} for marcasite, thus allowing confident mineral identification on this basis. Partitioning of trace elements between pyrite and marcasite was assessed by LA-ICP-MS images of the largest crystalline marcasite in the samples RB2-3806.55 and H3-1980. The results are shown in Figure 16.4. Marcasite compositions from the Kockatea Shale are distinguished by high contents of Mn (max 2.5 wt%), and higher Pb, Zn, and As, mainly concentrated in the rims of marcasite crystals. LA-ICP-MS spot analyses of iron bisulfides from Hovea Member, Ubara, and Meishan also reveal high Mn content (0.2–0.9 wt%) in crystals where marcasite was inferred, which contrasts with low Mn in pyrite (0.01–0.08 wt%) in the same samples.

16.4.4. Chemostratigraphy

Whole-rock chemostratigraphic analyses of Redback-2 and Hovea-3 samples (Table 16.2, Figs. 16.6 and 16.7) reveals several changes and anomalies across the interval between 3,807 and 3,806.5 m in Redback-2. The most notable anomaly recorded in Redback-2 is a negative shift in $\delta^{13}C_{org}$, from a stable average of -24.8‰ in the Permian mudstones below this interval, down to -32.35‰ within the interval. The isotopic composition remains around -31‰ for the next 4.5 m, and then increases to -27‰ by 3,801.7 m. This -6‰ shift in $\delta^{13}C_{org}$ in RB2 is very similar to the shift reported for Hovea-3 between 1,981 and 1,980.5 m depth (Thomas et al., 2004) and for other Permian-Triassic sequences across the globe (Metcalfe et al., 2014; Yin et al., 2012). Whole-rock sulphur isotopes display a ^{34}S-depleted signature and an "S"-shaped pattern, changing from strongly negative $\delta^{34}S$ during the Permian (-35 to -54‰) to less negative $\delta^{34}S$ in the Triassic (-22 to -29‰). This fits well with the global

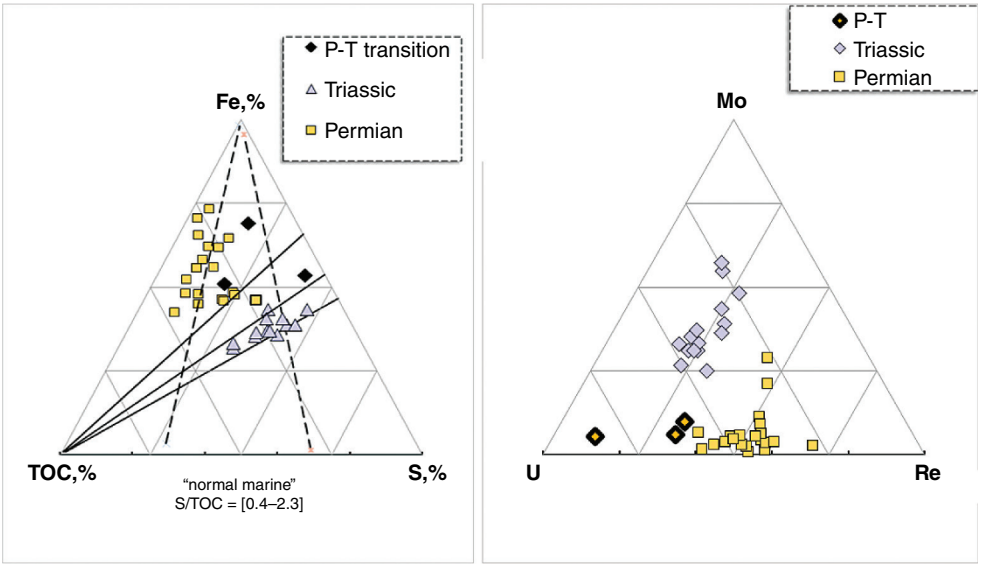

Figure 16.6 Variation in redox parameters-(Fe-S-TOC and Mo-Re-U), Hovea Member sediments from Redback-2 oil well.

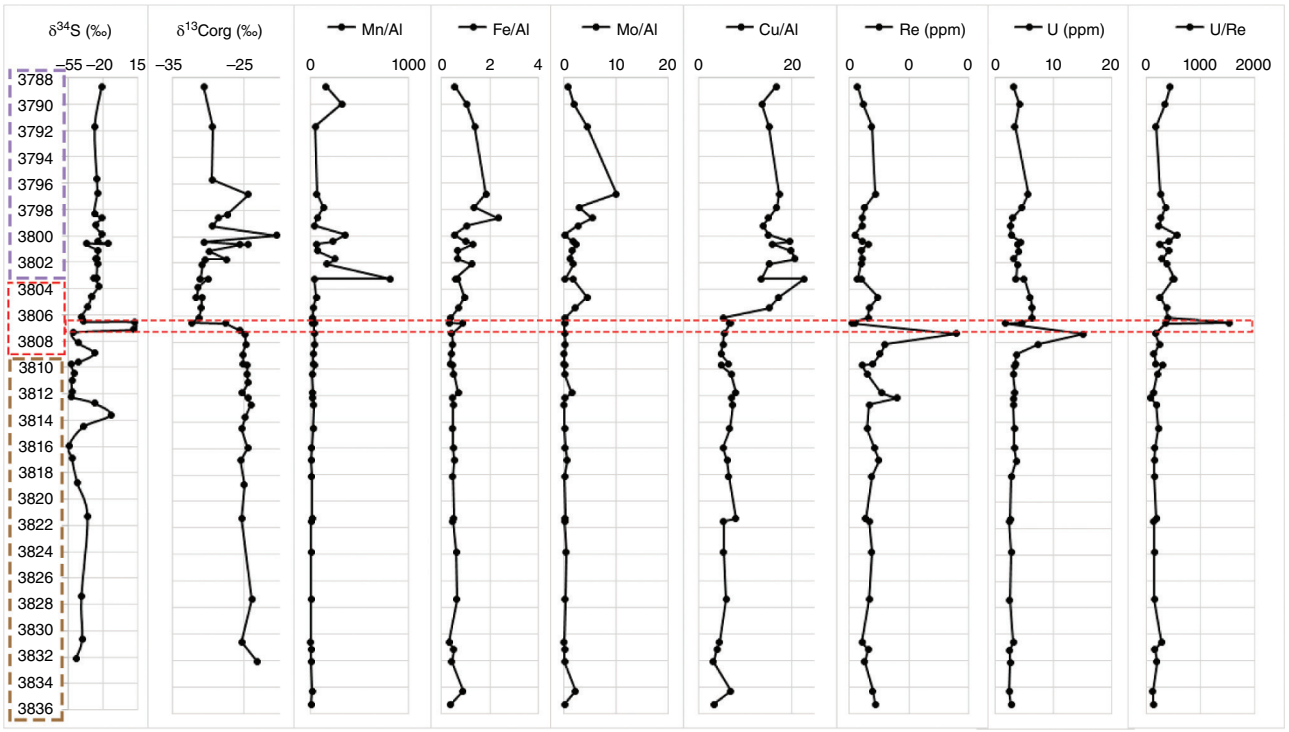

Figure 16.7 Chemostratigraphic parameters ($\delta^{34}S$, $\delta^{13}C$, and redox sensitive) in Hovea Member sediments from Redback-2 oil well.

pattern of $\delta^{34}S$ variations in sedimentary pyrite of the same age (Canfield et al., 2000; Canfield & Teske, 1996; Parnell et al., 2010).

A positive anomaly of $\delta^{34}S$ (11.2 ± 0.3‰) coincides with the sharp negative $\delta^{13}C_{org}$ at 3,807–3,806.5 m in RB2. Since marcasite and pyrite intergrowths were identified in these samples, we proceeded with assessing sulphur isotopes in-situ by SHRIMP-SI. The analyzed aggregate is composed of euhedral crystals of pyrite ~400 μm in diameter, with much smaller crystals of marcasite about 60 μm across concentrated on the margins of the larger pyrite crystals. However, there is no evidence of replacement of one mineral phase over another. Marcasite is characterized by a distinctly heavier, ^{34}S-enriched $\delta^{34}S$ signature (+2.7, +11.86, and +17.35‰) coupled with small positive and negative $\Delta^{33}S$ anomalies (+ 0.06, -0.04, and +0.01‰, respectively). Standard deviation (1 sigma) of the individual analyses on marcasite is slightly higher (0.04–0.41‰) than that on pyrite (0.07–0.11 ‰), which reveals marcasite higher isotopic heterogeneity on microscale. Pyrite associated with marcasite has much lighter and more homogenous isotopic ratios ($\delta^{34}S$ = −13.02 ± 0.06‰, standard deviation is for 4 analyses) (Table 16.3). We also analyzed pyrite from Opal Creek ($\delta^{34}S$ = −34 ± 3‰ standard deviation is for 9 analyses) and obtained a ^{34}S-depleted signature coupled to mainly positive $\Delta^{33}S$ anomalies (+0.07 ‰, n = 8), very similar to that reported previously by Zhang et al. (2017). In $\Delta^{33}S$ vs. $\delta^{34}S$ space (Fig. 16.5), our results for pyrite form a trend that is aligned along that between quantitative sulfate reduction toward sulphur disproportionation, whereas the marcasite signature extends into the field where mixed sulphur sources are the most plausible mechanism to explain its formation (Johnston et al., 2008; Tostevin et al., 2014).

Several whole-rock geochemical parameters considered to be paleoredox indicators (Fe, Mo, Cu, and Fe-S-TOC; Dean & Arthur, 1989; Tribovillard et al., 2006) change upward immediately after the $\delta^{13}C_{org}$ shift in Redback-2 mudstones. Mo/Al values display the most noticeable change (from an average of 0.36 below to 2.7 above), followed by Cu/Al values (from 6 to 17). The shift in carbon isotopic values is preceded by a five-fold increase in Re and U contents, observed at 3,807.35 m, that is, one meter below the carbon shift. A spike in the U/Re ratio (from a mean value of 260 to 1543) coincides with a $\delta^{13}C_{org}$ drop at 3,806.5 m. The organic carbon content in the Permian strata is generally low (1–3 wt% TOC) but drops abruptly to a very low level (<0.7 wt% TOC) in parallel with the carbon isotopic shift. Therefore, this lack of organic

carbon and admixture of iron sulfides produced an anomalously low TOC/(Fe+S) ratio in the $\delta^{13}C_{org}$ shift interval. In contrast, the Triassic sediments are relatively enriched in organic carbon (2–7 wt%).

16.5. DISCUSSION

16.5.1. Permian-Triassic Transition in the Perth Basin

Lithostratigraphy, palynology, and chemostratigraphy data for Hovea Member sediments in the Perth Basin suggest several major paleoenvironmental changes accompanied the Permian-Triassic transition. The transitional interval 3,807–3,806.5 m in the Redback-2 drill core can be clearly correlated with that of 1,982.3–1,980 m in the Hovea-3 drill core through a negative $\delta^{13}C_{org}$ shift, accompanied by a drop in organic carbon content and a simultaneous enrichment in distinctively heavier ^{34}S sulphur. Assuming the $\delta^{13}C_{org}$ is correlative to the EPME at 251.9 Ma, the extinction in the Perth Basin may correspond to the gap in calcite macrofossils and palynofacies, which precede the euxinic interval that developed later during the earliest Triassic transgression. The latter we infer from the redox indicators in RB2 sediments and it is consistent with previous studies of biomarkers in Hovea-3 (Grice et al., 2005a, 2005b, 2005c; Grice et al., 2007).

16.5.2. Marcasite Features and Probable Origin in the Permian-Triassic Sequences

The observed pyrite and marcasite banded crystals in the older layers suggest dynamic pH-Eh conditions during formation at or near the sediment-water interface, whereas euhedral overgrowths (cubic pyrite and marcasite blades) likely formed later during diagenesis. In such cases, seawater chemistry would have influenced marcasite formation and ocean acidification may be indicated. The ^{34}S-enriched signature of euhedral marcasite may result from a difference in timing between pyrite (earlier) and marcasite (later), if the latter were affected by Rayleigh distillation of pore water sulfate and restricted sulfate supply (Goldhaber & Kaplan, 1974). A similar process can be suggested for marcasite-dominated nodules in the upper Meishan clays. In contrast to the upper horizons, marcasite in the Bed MD-27 clay, 8 cm above the EPME interval and preceding volcanic Bed MD-28, is the likely metastable precursor for pyrite. The conversion of marcasite into pyrite from the rims toward the core implies a progressive pH increase in the pore water. In the deeper Panthalassic Ocean, represented by the cherts and shales from Ubara, the alternating marcasite-pyrite bands preserved in the sediment (earlier) and juxtaposed with coexisting euhedral pyrite and gypsum (later) may imply a variation of pH and rapidly fluctuating fluid chemistry at or just below the seafloor.

The Mn-rich marcasite also requires further evaluation. It may indicate a locally oxidizing environment during diagenesis, as pore water is commonly dominated by Mn^{3+} resulting from the oxidation of Mn^{2+} diffusing upward from anoxic sediments rather than from reduction of settling manganese oxides (Madison et al., 2013). Alternatively, higher Mn uptake into the iron sulfide structure may reflect a contribution of gaseous components. In support of this hypothesis, Mn-rich pyrite has been found in cold seepage environments (Shikazono et al., 1994), and marcasite nucleation is promoted by methane oxidation and pH drop (Xu, 2010), whereas higher sulfide production and manganese concentration in pore waters have been found in anoxic sediments containing natural gas (Ramírez-Pérez et al., 2015).

In summary, we propose that the near-simultaneous worldwide occurrence of likely diagenetic marcasite at or near the Permian-Triassic Boundary, associated with the main chemostratigraphic changes and anomalies related to the PTB, is very significant. The main arguments supporting this inference are as follows:

1. Marcasite from the Kockatea Shale spans the PTB interval and has an anomalous S isotopic composition. The enrichment of marcasite in ^{34}S coupled with negative $\Delta^{33}S$ suggests an additional source of sulphur that can be either of volcanic or riverine input, rather than extreme sulfate reduction in a pore water environment (Tostevin et al., 2014). Riverine input would be a logical source in a shallow environment, however, several authors have also documented local magmatic activity in the Perth Basin due to extensional tectonics during the transgression period across the PTB (Gorter et al., 2009; Veevers & Tewari, 1995), therefore volcanic sulphur addition cannot be absolutely excluded. Alternatively, acid rains from the distant LIP may also have served as a source of isotopically heavy S (Large et al., Chapter 15 this volume), as has been inferred from the recent O- and S-isotopic studies of gases in stratospheric plumes from active volcanoes (Martin, 2018).

2. Occasional analyses with a similar ^{33}S-^{34}S signature have been reported from different PTB localities: (a) the first study of sulphur isotopes in Meishan (Jiang et al., 2006) revealed the presence of isotopically heavy sulphur with a slightly positive $\delta^{34}S$ in microcrystals of euhedral pyrite from a layer near the PTB. These were interpreted to indicate pyrite growth from a closed porewater system in an anoxic sediment. (b) Among pyrite isotopic compositions in Meishan reported by Shen et al. (2011), one pyrite crystal from Bed 24, 9 cm below the

extinction Bed 25, had $\delta^{34}S = +2.88‰$ and $\Delta^{33}S = -0.049$ ‰. Mixing under conditions of enhanced sulfate-reduction rates relative to pore water sulfate supply have been suggested to explain that occurrence. (c) A heavy $\delta^{34}S$ value (+4 ‰) has been reported from Bed 24e at Meishan (Zhang et al., 2011). This occurrence has been attributed to the possible presence of larger framboids, likely related to later pore-water processes, in the analyzed framboidal separate from the euxinic interval. Also, three similar results have been reported for pyrites from about 1 m below the PTB in the Gujo-Hachiman section (Zhang et al., 2017). These have been explained as eventual shoaling of deeper sulfidic waters into shallower waters.

16.5.3. Marcasite From Other Stratigraphic Boundaries in Marine Sediments

Finally, we review marcasite occurrences of a range of ages reported in the literature. Schieber (2011) identified authigenic or early diagenetic euhedral micron-size marcasite in 11 Shale Units, including Devonian (Frasnian/Famenian) New Albany black shales and suggested multiple events of oxygenated bottom all through the sequence several meters thick. Abundant Mn-rich (1.1%) marcasite along with pyrite was identified in DSDP Leg 40 Site 364 within layers with no defined age (but possibly at the extinction horizon) between the Cenomanian and Upper Turonian pelagic biogenic calcareous strata (Siesser, 1978). The formation of radiating clusters and well-developed pyramidal marcasite crystals was explained by low pH (6.5) of the interstitial pore water. Another unusual combination of "pyrite" and gypsum was found in the same core in the Upper Miocene layer. It was concluded that generally reducing pyrite-forming environment was temporarily affected by pH "low enough to dissolve some planktonic calcareous organisms; the derived calcium combined with already present sulphate ions to form gypsum once the solubility of that mineral was exceeded" (Siesser, 1978). Borella (1984) described marcasite occurrence in Walvis Ridge Leg 74 Site 525, where marcasite nodules occur in slump beds and green turbidites alternating with red, brown, and white beds. Color variation was proposed to correlate with variable Eh in the sediment. In absence of iron sulfides in the red layers, marcasite in green turbidite was suggested to represent a reducing environment during a very short period of time (several hundred thousand years), particularly at the Cretaceous-Tertiary boundary, and not repeated elsewhere in the sequence. Finally, marcasite along with pyrite was identified in the Silurian (Wenlockian) Waldron Shale (Beier & Feldman, 1991). Different marcasite morphologies yielded different sulphur isotopic compositions, for example, prismatic ($\delta^{34}S = +0.0-5.0‰$) and "cockscomb" ($\delta^{34}S = +21.4$ to $+38.8‰$), which were both mostly higher than those of coexisting pyrite (−24.2 to +13.8‰). In each case, the marcasite occurrence was interpreted in agreement with the hydrothermal experimental framework, consistent with existing literature.

Next, we summarize in Table 16.4 the records noticing coincidences between the occurrence of marcasite in marine sediments, mass extinctions and LIP formation processes.

16.6. CONCLUSIONS

In this study, marcasite has been described in close association with the PTB in two shallow sedimentary sequences from the Paleo-Tethys and in one section representing the deep paleo-Panthalassic Ocean. Our results, and other published data, allow for a plausible diagenetic timing of formation for marcasite in each locality. Furthermore, some samples (i.e., those from the Kockatea Shale) contain evidence suggesting marcasite may have formed at the sediment-water interface in certain instances. Together, these results support the use of marcasite as a proxy for ocean pH. We further suggest that greater attention be given to petrography during studies of the PTB and other extinction-related stratigraphic intervals through geologic time in order to evaluate whether diagenetic marcasite is present. As stated by Schieber (2011), early diagenetic "marcasite formation, accompanied by redox shifts, low pH, and sulfide dissolution, has a clear potential to substantially alter trace-metal-based paleo-oceanographic proxies." It can also provide us with information concerning the magnitude of changes to the ocean-atmosphere system during times of environmental crisis.

ACKNOWLEDGMENTS

This work is supported by Australian Research Council Discovery (ARC) grant to R. Large (DP 150102578). K. Grice acknowledges ARC for DORA (number) and DP (number) for this work. We thank the GSWA core library for assistance with sample collection. We thank Prof. C. M. Henderson for sharing his understanding of the depositional time frame of the Opal Creek succession. We thank A. Cuison and M. Chapple for sample preparation; S. Stepanov, P. Olin, and S. Gilbert for technical assistance for LA-ICP-MS analysis; I. Muhkerjee, D. Gregory, and J. Avila for formal analysis by SHRIMP and fruitful discussion of the paper. We also appreciate the wise comments from Yadong Sun and an anonymous reviewer of the manuscript. In addition, we thank S. Stepanov for XRD analysis of siderite sample.

Table 16.4 Records About Marcasite Occurrence From Several Stratigraphic Boundaries in Phanerozoic Temporally Linked to Mass Extinctions and/or to the Large Igneous Province Activity

Locality	Age	Lithology	Marcasite morphology	Source	Mass extinction	LIP	Source
Walvis Ridge LEG 74 site 525	Cretaceous - Tertiary	Green turbidite	Nodules	Borella, 1984	K/T, massive	Deccan Traps; ocean plateau	Buchs, 2018
DSDP LEG 40 site 364	Cretaceous (Cenomanian-Turonian)	CB5-T2 Siliceous pelagic biogenic calcareous firm nannofossil chalk	Pyramidal and radiating clusters, Mn-rich	Siesser, 1978	Bonarelli event (or OAE2)	High Arctic (HALIP)	Schröder-Adams et al., 2019
Southern Hess Rise Hole 465	Cretaceous (Albian - Cenomanian)	Sulfide layer A-40-1, 126-129 cm in limestone with abundant volcanic ash overlaying trachyte volcanic breccia	Associated with pyrite and barite	Koski & Hein, 1981			
Opal Creek	Permian-Triassic	Black shale; sulfide layer	Isometric crystals intergrown with pyrite	Schoepfer et al., 2013; This study	EPME	Siberian Traps (STLIP)	
Kockatea Shale	Permian - Triassic	Black shales; fossiliferous shales	Intergrown with pyrite; euhedral, isometric and elongated blades; Mn-rich	This study	EPME	STLIP; Regional magmatism?	
Ubara	Permian - Triassic	shales, cherts, and sulfide layer	Intergrown with pyrite; fine bands alternating with pyrite and euhedral	This study; Algeo et al., 2011; Schoepfer et al., 2013	EPME	STLIP	
Meishan	Permian - Triassic	shales , clays	Intergrown with pyrite; Mn-rich	This study	EPME	STLIP	
New Albany	Devonian (Famenian-Frasenian)	Black shales, ~40 m thick	Clusters of equant euhedral grains or aggregates of tabular crystals	Schieber, 2011	The Late Devonian	Viluy Traps and/or intraplate PDD magmatism	Bond & Wignall, 2014; Courtillot et al., 2010
Waldron Shale	Silurian (Wenlockian)	Shale	Prismatic and cockscomb	Beier & Feldman, 1991	Llandovery-Wenlock series boundary ?	?	Calner, 2008

REFERENCES

Algeo, T. J., Kuwahara, K., Sano, H., Bates, S., Lyons, T., Elswick, E., Hinnov, L., et al. (2011). Spatial variation in sediment fluxes, redox conditions, and productivity in the Permian-Triassic Panthalassic Ocean. *Palaeogeography, Palaeoclimatology, Palaeoecology*, *308*(1–2), 65–83.

Allen, E. T., Crenshaw, J. L., Johnston, J., & Larsen, E. S. (1912). The mineral sulphides of iron; with crystallographic study by E. S. Larsen. American Journal of Science, *s4-33*(195), 169–236. https://doi.org/10.2475/ajs.s4-33.195.169.

Beier, J. A., & Feldman, H. R. (1991). Sulphur isotopes and paragenesis of sulfide minerals in the Silurian Waldron Shale, southern Indiana. *Geology, 19*(4), 389–392. doi: 10.1130/0091-7613(1991)019<0389:SIAPOS>2.3.CO;2

Belousov, I. (2014). *New calibration standard for LA-ICPMS analysis of sulphides*. AGU, 2014 Fall Meeting. https://agu.confex.com/agu/fm14/webprogram/Paper19453.html

Belousov, I., Danyushevsky, L., Olin, P., Gilbert, S., & Thompson, J. (2015). *STDGL3: A new calibration standard for sulphide analysis by LAICP-MS*. Goldschmidt 2015.

Berner, R. A. (1984). Sedimentary pyrite formation: An update. *Geochimica et Cosmochimica Acta, 48*(4), 605–615.

Black, B. A., Lamarque, J.-F., Shields, C. A., Elkins-Tanton, L. T., & Kiehl, J. T. (2013). Acid rain and ozone depletion from pulsed Siberian Traps magmatism. *Geology, 42*(1), 67–70. https://doi.org/10.1130/G34875.1

Blakey, R. C., & Ranney, W. D. (2018). The amalgamation of Pangaea and the Sonoma orogeny: Early Permian to Early Triassic, ca. 300–240 Ma. In *Ancient landscapes of western North America* (pp. 83–88). Springer, Cham

Bond, D. P. G., & Grasby, S. E. (2017). On the causes of mass extinctions. *Palaeogeography, Palaeoclimatology, Palaeoecology, 478*, 3–29. https://doi.org/10.1016/j.palaeo.2016.11.005

Bond, D. P. G., & Wignall, P. B. (2014). Large igneous provinces and mass extinctions: An update. In G. Keller & A. C. Kerr (eds.), *Volcanism, impacts, and mass extinctions: Causes and effects* (pp. 27–55). Geological Society of America Special Paper 505. https://doi.org/10.1130/2014.2505(02)

Borella, P. E. (1984). *Sedimentology, petrology, and cyclic sedimentation patterns, Walvis Ridge Transect, Leg-74, Deep-Sea Drilling Project*. Initial Reports of the Deep Sea Drilling Project *74* (Mar), 645–662.

Bryan, S. E., & Ferrari, L. (2013). Large igneous provinces and silicic large igneous provinces: Progress in our understanding over the last 25 years. *Geological Society of America Bulletin, 125*(7–8), 1053–1078. https://doi.org/10.1130/B30820.1

Buchs, D. M., Kerr, A. C., Brims, J. C., Zapata-Villada, J. P., Correa-Restreo, T., Rodríguez, G. (2018). Evidence for subaerial development of the Caribbean oceanic plateau in the Late Cretaceous and palaeo-environmental implications. *Earth and Planetary Science Letters, 499*, 62–73. https://doi.org/10.1016/j.epsl.2018.07.020

Burgess, S. D., & Bowring, S. A. (2015). High-precision geochronology confirms voluminous magmatism before, during, and after Earth's most severe extinction. *Science Advances, 1*(7), e1500470–e1500470. https://doi.org/10.1126/sciadv.1500470

Burgess, S. D., Bowring, S., & Shen, S. (2014). High-precision timeline for Earth's most severe extinction. *Proceedings of the National Academy of Sciences (U.S.A.), 111*(9), 3316–3321. https://doi.org/10.1073/pnas.1317692111

Burgess, S. D., Muirhead, J. D., & Bowring, S. A. (2017). Initial pulse of Siberian Traps sills as the trigger of the end-Permian mass extinction. *Nature Communications, 8*(1), art. 164. https://doi.org/10.1038/s41467-017-00083-9

Bush, R. T., McGrath, R., & Sullivan, L. A. (2004). Occurrence of marcasite in an organic-rich Holocene estuarine mud. *Soil Research, 42*(6), 617–621. https://doi.org/10.1071/SR03079

Cabral, R. A., Jackson, M. G., Rose-Koga, E. F., Koga, K. T., Whitehouse, M. J., Antonelli, M. A., Farquhar, J., et al. (2013). Anomalous sulphur isotopes in plume lavas reveal deep mantle storage of Archaean crust. *Nature, 496,* art. 490. https://doi.org/10.1038/nature12020

Calner, M. (2008). Silurian global events: At the tipping point of climate change. In *Mass extinction* (pp. 21–57). Berlin, Heidelberg: Springer. https://doi.org/10.1007/978-3-540-75916-4_4

Canfield, D. E., & Teske, A. (1996). Late Proterozoic rise in atmospheric oxygen concentration inferred from phylogenetic and sulphur-isotope studies. *Nature, 382,* 127–132. https://doi.org/10.1038/382127a0

Canfield, D. E., Habicht, K. S., & Thamdrup, B. (2000). The Archean sulphur cycle and the early history of atmospheric oxygen. *Science, 288*(5466), 658–661. doi: 10.1126/science.288.5466.658

Cawood, P. A., & Nemchin, A. A. (2000). Provenance record of a rift basin: U/Pb ages of detrital zircons from the Perth Basin, Western Australia. *Sedimentary Geology, 134*(3–4), 209–234. https://doi.org/10.1016/S0037-0738(00)00044-0

Cawood, P. A., & Nemchin, A. A. (2001). Paleogeographic development of the east Laurentian margin: Constraints from U-Pb dating of detrital zircons in the Newfoundland Appalachians. *Geological Society of America Bulletin, 113*(9), 1234-1246. https://doi.org/10.1130/0016-7606(2001)113<1234:PDOTEL>2.0.CO;2

Chen, Z.-Q., Yang, H., Luo, M., Benton, M. J., Kaiho, K., Zhao, L., Huang, Y., et al. (2015). Complete biotic and sedimentary records of the Permian-Triassic transition from Meishan section, South China: Ecologically assessing mass extinction and its aftermath. *Earth-Science Reviews, 149,* 67–107. https://doi.org/10.1016/j.earscirev.2014.10.005

Clarkson, M. O., Kasemann, S. A., Wood, R. A., Lenton, T. M., Daines, S. J., Richoz, S., Ohnemueller, F., et al. (2015). Ocean acidification and the Permo-Triassic mass extinction. *Science, 348*(6231), 229–232. https://doi.org/10.1126/science.aaa0193

Courtillot, V., & Fluteau, F. (2014). A review of the embedded time scales of flood basalt volcanism with special emphasis on dramatically short magmatic pulses. In G. Keller, & A. C. Kerr (Eds.), *Volcanism, impacts, and mass extinctions: Causes and effects* (pp. 301–317). Geological Society of America Special Paper 505. https://doi.org/10.1130/2014.2505(15)

Courtillot, V., et al. (2010). Preliminary dating of the Viluy traps (Eastern Siberia): Eruption at the time of Late Devonian extinction events? *Earth and Planetary Science Letters, 300*(3): 239–245. https://doi.org/10.1016/j.epsl.2010.09.045

Danyushevsky, L., Robinson, P., Gilbert, S., Norman, M., Large, R., McGoldrick, P., & Shelley, M. (2011). Routine

quantitative multi-element analysis of sulphide minerals by laser ablation ICP-MS: Standard development and consideration of matrix effects. *Geochemistry: Exploration, Environment, Analysis, 11*(1), 51–60. https://doi.org/10.1144/1467-7873/09-244

Dean, W. E., & Arthur, M. A. (1989). Iron-sulphur-carbon relationships in organic-carbon-rich sequences I: Cretaceous Western Interior seaway. *American Journal of Science, 289*(6), 708–743.

Doney, S. C., Fabry, V. J., Feely, R. A., & Kleypas, J. A. (2009). Ocean acidification: The other CO_2 problem. *Annual Review of Marine Science, 1,* 169–192. https://doi.org/10.1146/annurev.marine.010908.163834

Dustira, A. M., Wignall, P. B., Joachimski, M., Blomeier, D., Hartkopf-Fröder, C., & Bond, D. P. G. G. (2013). Gradual onset of anoxia across the Permian-Triassic Boundary in Svalbard, Norway. *Palaeogeography, Palaeoclimatology, Palaeoecology, 374,* 303–313. https://doi.org/10.1016/j.palaeo.2013.02.004

Ernst, R. E. (2014). *Large igneous provinces*. Cambridge: Cambridge University Press. https://doi.org/10.1017/CBO9781139025300

Ernst, R. E., & Youbi, N. (2017). How Large Igneous Provinces affect global climate, sometimes cause mass extinctions, and represent natural markers in the geological record. *Palaeogeography, Palaeoclimatology, Palaeoecology, 478,* 30–52. https://doi.org/10.1016/J.PALAEO.2017.03.014

Georgiev, S. V., Horner, T. J., Stein, H. J., Hannah, J. L., Bingen, B., & Rehkämper, M. (2015). Cadmium-isotopic evidence for increasing primary productivity during the Late Permian anoxic event. *Earth and Planetary Science Letters*, *410*, 84–96.

Gilbert, S. E., Danyushevsky, L. V., Rodemann, T., Shimizu, N., Gurenko, A., Meffre, S., Thomas, H., et al. (2014). Optimisation of laser parameters for the analysis of sulphur isotopes in sulphide minerals by laser ablation ICP-MS. *Journal of Analytical Atomic Spectrometry, 29*(6), 1042. https://doi.org/10.1039/c4ja00011k

Glasspool, I. J., & Scott, A. C. (2010). Phanerozoic concentrations of atmospheric oxygen reconstructed from sedimentary charcoal. *Nature Geoscience, 3*(9), 627–630. https://doi.org/10.1038/ngeo923

Goldhaber, M. B., & Kaplan, I. R. (1974) The sulphur cycle. In Goldberg (ed.), *Marine chemistry* (pp. 569–655). New York: John Wiley.

Goldschmidt (2015). Abstracts 251. https://goldschmidtabstracts.info/2015/251.pdf

Gorter, J. D., & Deighton, I. (2002). *Effects of igneous activity in the offshore northern Perth Basin: Evidence from petroleum exploration wells, 2D seismic and magnetic surveys*. Western Australian Basins Symposium III, 875–900.

Gorter, J. D., Nicoll, R. S., & Metcalfe, I. (2009). The Permian-Triassic boundary in western Australia, evidence from the Bonaparte and northern Perth basins: Exploration implications. *The APPEA Journal, 49*(1), 311–336.

Grant, H. L. J., Hannington, M. D., Petersen, S., Frische, M., & Fuchs, S. H. (2018). Constraints on the behavior of trace elements in the actively-forming TAG deposit, Mid-Atlantic Ridge, based on LA-ICP-MS analyses of pyrite. *Chemical Geology, 498*, 45–71. https://doi.org/10.1016/j.chemgeo.2018.08.019

Grice, K., Cao, C., Love, G. D., Böttcher, M. E., Twitchett, R. J., Grosjean, E., Summons, R. E., et al. (2005a). Photic zone euxinia during the Permian-triassic superanoxic event. *Science, 307*(5710), 706–709. https://doi.org/10.1126/science.1104323

Grice, K., Nabbefeld, B., & Maslen, E. (2007). Source and significance of selected polycyclic aromatic hydrocarbons in sediments (Hovea-3 well, Perth Basin, Western Australia) spanning the Permian-Triassic boundary. *Organic Geochemistry, 38,* 1795–1803. https://doi.org/10.1016/j.orggeochem.2007.07.001

Grice, K., Summons, R. E., Grosjean, E., Twitchett, R. J., Dunning, W., Wang, S. X., & Böttcher, M. E. (2005b). Depositional conditions of the northern onshore Perth Basin (basal Triassic). *The APPEA Journal, 45*(1), 262–274.

Grice, K., Twitchett, R. J., Alexander, R., Foster, C. B., & Looy, C. (2005c). A potential biomarker for the Permian-Triassic ecological crisis. *Earth and Planetary Science Letters, 236*(1–2), 315–321. https://doi.org/10.1016/j.epsl.2005.05.008

Grotheer, H., Le Métayer, P., Piggott, M. J., Lindeboom, E. J., Holman, A. I., Twitchett, R. J., & Grice, K. (2017). Occurrence and significance of phytanyl arenes across the Permian-Triassic boundary interval. *Organic Geochemistry, 104*, 42–52. http://dx.doi.org/10.1016/j.orggeochem.2016.12.002

Hinojosa, J. L., Brown, S. T., Chen, J., DePaolo, D. J., Paytan, A., Shen, S., & Payne, J. L. (2012). Evidence for end-Permian ocean acidification from calcium isotopes in biogenic apatite. *Geology, 40*(8), 743–746. https://doi.org/10.1130/G33048.1

Hofmann, G. E., Barry, J. P., Edmunds, P. J., Gates, R. D., Hutchins, D. A., Klinger, T., & Sewell, M. A. (2010). The effect of ocean acidification on calcifying organisms in marine ecosystems: an organism-to-ecosystem perspective. *Annual Review of Ecology, Evolution, and Systematics, 41*(1), 127–147. https://doi.org/10.1146/annurev.ecolsys.110308.120227

Hood, A. , Planavsky, N. J., Wallace, M. W., & Wang, X. (2018). The effects of diagenesis on geochemical paleoredox proxies in sedimentary carbonates. *Geochimica et Cosmochimica Acta, 232*, 265–287. https://doi.org/10.1016/J.GCA.2018.04.022

Hovea-3 Completion Report (2003). Origin LTD, 2003.

Ireland, T. R., Clement, S., Compston, W., Foster, J. J., Holden, P., Jenkins, B., Lanc, P., et al. (2008). Development of SHRIMP. *Australian Journal of Earth Sciences, 55*(6–7), 937–954.

Isozaki, Y. (1997). Permo-Triassic boundary superanoxia and stratified superocean: Records from lost deep sea. *Science, 276*(5310), 235–238. https://doi.org/10.1126/science.276.5310.235

Jafary Dargahi, H. J. (2014). *Shale gas prospectivity studies in the Perth Basin, Western Australia*. Ph.D. Thesis. School of Chemical and Petroleum Engineering, Department of Petroleum Engineering. Curtin University. https://espace.curtin.edu.au/handle/20.500.11937/453

Jiang, Y. F., Tang, Y. G., & Chou, C. L. (2006). Research on genesis of pyrite near the Permian-Triassic Boundary in Meishan, Zhejiang, China. *Journal of China University of Mining and Technology, 16*(4), 457–460. https://doi.org/http://dx.doi.org/10.1016/S1006-1266(07)60047-9

Jin, Y., Wang, Y., Henderson, C., Wardlaw, B. R., Shen, S., & Cao, C. (2006). The Global Boundary Stratotype Section and Point (GSSP) for the base of Changhsingian Stage (Upper

Permian). *Episodes, 29*(3), 175–182. https://pubs.er.usgs.gov/publication/70028427

Jochum, K. P. (2014). *Reference materials in geochemical and environmental research. analytical geochemistry/inorganic instrumental analysis* (2nd ed., Vol. 15). Elsevier Ltd. https://doi.org/10.1016/B978-0-08-095975-7.01403-0

Johnston, D. T., Farquhar, J., Habicht, K. S., & Canfield, D. E. (2008). Sulphur isotopes and the search for life: Strategies for identifying sulphur metabolisms in the rock record and beyond. *Geobiology, 6*(5), 425–435. https://doi.org/10.1111/j.1472-4669.2008.00171.x

Jones, A. T. (2011). New exploration opportunities in the offshore northern Perth Basin. *The APPEA Journal, 51*(1), 45–78.

Jurikova, H., Liebetrau, V., Gutjahr, M., Rollion-Bard, C., Hu, M. Y., Krause, S., Henkel, D., et al. (2019). Boron isotope systematics of cultured brachiopods: Response to acidification, vital effects and implications for palaeo-pH reconstruction. *Geochimica et Cosmochimica Acta, 248*, 370–386. https://doi.org/10.1016/j.gca.2019.01.015

Kerr, A. C. (1998). Oceanic plateau formation: A cause of mass extinction and black shale deposition around the Cenomanian-Turonian boundary? *Journal of the Geological Society, 155*(4), 619–626. https://doi.org/10.1144/gsjgs.155.4.0619

Kidder, D. L., & Worsley, T. R. (2010). Phanerozoic large igneous provinces (LIPs), HEATT (haline euxinic acidic thermal transgression) episodes, and mass extinctions. *Palaeogeography, Palaeoclimatology, Palaeoecology, 295*(1–2), 162–191. https://doi.org/10.1016/j.palaeo.2010.05.036

Koski, R. A., & Hein, J. R. (1981). *Petrographic and chemical characteristics of pyrite-marcasite mineralization in Hole 465A, Southern Hess Rise*. IODP Initial Reports of the Deep Sea Drilling Project, Volume 62. doi:10.2973/dsdp.proc.62.141.1981

Kravchinsky, V. A. (2012). Paleozoic large igneous provinces of Northern Eurasia: Correlation with mass extinction events. *Global and Planetary Change, 86–87*, 31–36. https://doi.org/10.1016/J.GLOPLACHA.2012.01.007

Large, R. R., Halpin, J. A., Danyushevsky, L. V., Maslennikov, V. V., Bull, S. W., Long, J. A., Gregory, D. D., et al. (2014). Trace element content of sedimentary pyrite as a new proxy for deep-time ocean-atmosphere evolution. *Earth and Planetary Science Letters, 389,* 209–220.

Liang, H. (2002) End-Permian catastrophic event of marine acidification by hydrated sulphuric acid: Mineralogical evidence from Meishan section of South China. *Chinese Science Bulletin, 47,* 1393–1397.

Lin, Z., Sun, X., Lu, Y., Xu, L., Gong, J., Lu, H., & Teichert, B. M. A. (2016). Stable isotope patterns of coexisting pyrite and gypsum indicating variable methane flow at a seep site of the Shenhu area, South China Sea. *Journal of Asian Earth Sciences, 123*, 213–223. https://doi.org/10.1016/j.jseaes.2016.04.007

Madison, A. S., Tebo, B. M., Mucci, A., Sundby, B., & Luther, G. W. (2013). Abundant porewater Mn(III) is a major component of the sedimentary redox system. *Science, 341*(6148), 875–878. https://doi.org/10.1126/science.1241396

Martin, E. (2018). Volcanic plume impact on the atmosphere and climate: O- and S-isotope insight into sulfate aerosol formation. *Geosciences, 8*(6), art. 198. https://doi.org/10.3390/geosciences8060198

Melekestseva, I., Maslennikov, V., Safina, N., Nimis, P., Maslennikova, S., Beltenev, V., Rozhdestvenskaya, I., et al. (2018). Sulfide breccias from the Semenov-3 Hydrothermal Field, Mid-Atlantic Ridge: Authigenic mineral formation and trace element pattern. *Minerals, 8*(8), art. 321. https://doi.org/10.3390/min8080321

Metcalfe, I., Crowley, J. L., Nicoll, R. S., & Schmitz, M. (2014). High-precision U-Pb CA-TIMS calibration of Middle Permian to Lower Triassic sequences, mass extinction and extreme climate-change in eastern Australian Gondwana. *Gondwana Research, 28*(1), 61–81. https://doi.org/10.1016/j.gr.2014.09.002

Meyers, P. A. (2014). Why are the $\delta^{13}C_{org}$ values in Phanerozoic black shales more negative than in modern marine organic matter? *Geochemistry, Geophysics, Geosystems, 15*(7), 3085–3106. https://doi.org/10.1002/2014GC005305

Murowchick, J. B., & Barnes, H. L. (1986). Marcasite precipitation from hydrothermal solutions. *Geochimica et Cosmochimica Acta, 50*(12), 2615–2629. https://doi.org/10.1016/0016-7037(86)90214-0

Nabbefeld, B., Grice, K., Schimmelmann, A., Sauer, P. E., Böttcher, M. E., & Twitchett, R. (2010). Significance of $\delta D_{kerogen}$, $\delta^{13}C_{kerogen}$ and $\delta^{34}S_{pyrite}$ from several Permian/Triassic (P/Tr) sections. *Earth and Planetary Science Letters, 295*(1–2), 21–29.

Newhouse, W. H. (1925). Paragenesis of marcasite. *Economic Geology, 20*(1), 54–66. https://doi.org/10.2113/gsecongeo.20.1.54

Ono, S., Shanks, W. C., Rouxel, O. J., & Rumble, D. (2007). S-33 constraints on the seawater sulfate contribution in modern seafloor hydrothermal vent sulfides. *Geochimica et Cosmochimica Acta, 71*(5), 1170–1182. https://doi.org/10.1016/j.gca.2006.11.017

Parnell, J., Boyce, A., Thackrey, S., Muirhead, D., Lindgren, P., Mason, C., Taylor, C., et al. (2010). Sulphur isotope signatures for rapid colonization of an impact crater by thermophilic microbes. *Geology, 38*(3), 271–274. https://doi.org/10.1130/G30615.1

Payne, J. L., Turchyn, A. V., Paytan, A., DePaolo, D. J., Lehrmann, D. J., Yu, M., & Wei, J. (2010). Calcium isotope constraints on the end-Permian mass extinction. *Proceedings of the National Academy of Sciences (U.S.A.), 107*(19), 8543–8548. https://doi.org/10.1073/pnas.0914065107

Pettijohn, F. J. (1957). *Sedimentary rocks, 2nd ed*. New York: Harper & Row.

Phipps, D., & Playford, G. (1984). Laboratory techniques for extraction of palynomorphs from sediments. *Papers of the Department of Geology, University of Queensland, 11*(1), 1–23. http://espace.library.uq.edu.au/view/UQ:179170

Qian, G., Xia, F., Brugger, J., Skinner, W. M., Bei, J., Chen, G., & Pring, A. (2011). Replacement of pyrrhotite by pyrite and marcasite under hydrothermal conditions up to 220 °C: An experimental study of reaction textures and mechanisms. *American Mineralogist, 96*(11–12), 1878–1893. https://doi.org/10.2138/am.2011.3691

Ramírez-Pérez, A. M., de Blas, E., & García-Gil, S. (2015). Redox processes in pore water of anoxic sediments with

shallow gas. *Science of the Total Environment, 538*, 317–326. https://doi.org/10.1016/j.scitotenv.2015.07.111.

Redback-2 Completion Report (2010). Origin LTD, 2010.

Rickard, D. (2012). The evolution of the sedimentary sulphur cycle. In *Developments in sedimentology (Vol. 65)*. Elsevier Science Ltd. https://doi.org/10.1016/B978-0-444-52989-3.00017-9

Roberts, J., Kaczmarek, K., Langer, G., Skinner, L. C., Bijma, J., Bradbury, H., Turchyn, A. V., et al. (2018). Lithium isotopic composition of benthic foraminifera: A new proxy for paleo-pH reconstruction. *Geochimica et Cosmochimica Acta, 236*, 336–350. https://doi.org/10.1016/J.GCA.2018.02.038

Rouxel, O., Fouquet, Y., & Ludden, J. N. (2004). Subsurface processes at the lucky strike hydrothermal field, Mid-Atlantic ridge: Evidence from sulphur, selenium, and iron isotopes. *Geochimica et Cosmochimica Acta, 68*(10), 2295–2311. https://doi.org/10.1016/j.gca.2003.11.029

Schieber, J. (2011). Marcasite in black shales: A mineral proxy for oxygenated bottom waters and intermittent oxidation of carbonaceous muds. *Journal of Sedimentary Research, 81*(7), 447–458. https://doi.org/10.2110/jsr.2011.41

Schoepfer, S. D., Henderson, C. M., Garrison, G. H., & Ward, P. D. (2012). Cessation of a productive coastal upwelling system in the Panthalassic Ocean at the Permian-Triassic Boundary. *Palaeogeography, Palaeoclimatology, Palaeoecology, 313–314*, 181–188. https://doi.org/10.1016/j.palaeo.2011.10.019

Schoepfer, S. D., Henderson, C. M., Garrison, G. H., Foriel, J., Ward, P. D., Selby, D., Hower, J. C., et al. (2013). Termination of a continent-margin upwelling system at the Permian-Triassic boundary (Opal Creek, Alberta, Canada). *Global and Planetary Change, 105*, 21–35. http:// 10.1016/j.gloplacha.2012.07.005

Schoonen, M. A. A. (2004). Mechanisms of sedimentary pyrite formation. In J. P. Amend, K. J. Edwards, & T. W. Lyons (Eds.), *Sulphur biogeochemistry: Past and present* (pp. 117–134). Geological Society of America, Special Paper 379. https://doi.org/10.1130/0-8137-2379-5.117

Schoonen, M. A. A., & Barnes, H. L. (1991a). Mechanisms of pyrite and marcasite formation from solution: III. Hydrothermal processes. *Geochimica et Cosmochimica Acta, 55*(12), 3491–3504. https://doi.org/10.1016/0016-7037(91)90050-F

Schoonen, M. A. A., & Barnes, H. L. (1991b). Reactions forming pyrite and marcasite from solution: I. Nucleation of FeS_2 below 100°C. *Geochimica et Cosmochimica Acta, 55*(6), 1495–1504. https://doi.org/10.1016/0016-7037(91)90122-L

Schoonen, M. A. A., & Barnes, H. L. (1991c). Reactions forming pyrite and marcasite from solution: II. Via FeS precursors below 100°C. *Geochimica et Cosmochimica Acta, 55*(6), 1505–1514. https://doi.org/10.1016/0016-7037(91)90123-M

Schröder-Adams, C. J., Herrle, J. O., Selby, D., Quesnel, A., & Froude, G. (2019). Influence of the High Arctic Igneous Province on the Cenomanian/Turonian boundary interval, Sverdrup Basin, High Canadian Arctic. *Earth and Planetary Science Letters, 511*, 76–88. doi.org/10.1016/j.epsl.2019.01.023

Scott, R. J., Meffre, S., Woodhead, J., Gilbert, S. E., Berry, R. F., & Emsbo, P. (2009). Development of framboidal pyrite during diagenesis, low-grade regional metamorphism, and hydrothermal alteration. *Economic Geology, 104*(8), 1143–1168. https://doi.org/10.2113/gsecongeo.104.8.1143

Shen, S., Ramezani, J., Chen, J., Cao, C. Q, Erwin, D. H., Zhang, H., Xiang, L., et al. (2019). A sudden end-Permian mass extinction in South China. *GSA Bulletin, 131*(1–2), 205–223. doi: https://doi.org/10.1130/B31909.1

Shen, Y. A., Farquhar, J., Zhang, H., Masterson, A., Zhang, T. G., & Wing, B. A. (2011). Multiple S-isotopic evidence for episodic shoaling of anoxic water during Late Permian mass extinction. *Nature Communications, 2*(1), art. 210. https://doi.org/10.1038/ncomms1217

Shi, G. R., Waterhouse, J. B., & McLoughlin, S. (2010). The Lopingian of Australasia: A review of biostratigraphy, correlations, palaeogeography and palaeobiogeography. *Geological Journal, 45*(2–3), 230–263. https://doi.org/10.1002/gj.1213

Shikazono, N., Nakata, M., & Tokuyama, E. (1994). Pyrite with high Mn content from the Nankai Trough formed from subduction-induced cold seepage. *Marine Geology, 118*(3–4), 303–313. https://doi.org/10.1016/0025-3227(94)90090-6

Siesser, W. G. (1978). Petrography and geochemistry of pyrite and marcasite in Deep Sea Drilling Project Leg 40 sediments. In H. M. Bolli et al. (Eds.), *Init. Repts. DSDP, Suppl. to Vols. 38, 39, 40, and 41* (pp. 767–775). Washington: U.S. Govt. Printing Office.

Spaak, G., Edwards, D. S., Allen, H. J., Grotheer, H., Summons, R. E., Coolen, M. J. L., & Grice, K. (2018). Extent and persistence of photic zone euxinia in Middle-Late Devonian seas: Insights from the Canning Basin and implications for petroleum source rock formation. *Marine and Petroleum Geology, 93,* 33–56. https://doi.org/10.1016/j.marpetgeo.2018.02.033

Steadman, J., & Large, R.R. (2016). Synsedimentary, diagenetic, and metamorphic pyrite, pyrrhotite, and marcasite at the Homestake BIF-Hosted Gold Deposit, South Dakota, USA: Insights on Au-As ore genesis from textural and LA-ICP-MS trace element studies. *Economic Geology, 111*(7), 1731–1752. https://doi.org/10.2113/econgeo.111.7.1731

Thomas, B. M., Willink, R. J., Grice, K., Twitchett, R. J., Purcell, R. R., Archbold, N. W., George, A. D., et al. (2004). Unique marine Permian-Triassic boundary section from Western Australia. *Australian Journal of Earth Sciences, 51*(3), 423–430. https://doi.org/10.1111/j.1400-0952.2004.01066.x

Thomas, H. V., Large, R. R., Bull, S. W., Maslennikov, V., Berry, R. F., Fraser, R., Froud, S., et al. (2011). Pyrite and pyrrhotite textures and composition in sediments, laminated quartz veins, and reefs at Bendigo Gold Mine, Australia: Insights for ore genesis. *Economic Geology, 106*, 1–31. https://doi:10.2113/econgeo.106.1.1

Tossell, J. A., Vaughan, D. J., & Burdett, J. K. (1981). Pyrite, marcasite, and arsenopyrite type minerals: Crystal chemical and structural principles. *Physics and Chemistry of Minerals, 7*(4), 177–184. https://doi.org/10.1007/BF00307263

Tostevin, R., Turchyn, A. V., Farquhar, J., Johnston, D. T., Eldridge, D. L., Bishop, J. K. B., & McIlvin, M. (2014). Multiple sulphur isotope constraints on the modern sulphur cycle. *Earth and Planetary Science Letters, 396*, 14–21. https://doi.org/http://dx.doi.org/10.1016/j.epsl.2014.03.057.

Traverse, A. (2007). *Paleopalynology, 2nd ed*. Topics in Geobiology (Vol. 28). Berlin, Springer. Tribovillard, N.,

Algeo, T. J., Lyons, T., & Riboulleau, A. (2006). Trace metals as paleoredox and paleoproductivity proxies: An update. *Chemical Geology, 232*(1–2), 12–32. https://doi.org/10.1016/j.chemgeo.2006.02.012

Veevers, J. J., & Tewari, R. C. (1995). Permian-Carboniferous and Permian-Triassic magmatism in the rift zone bordering the Tethyan margin of southern Pangea. *Geology, 23*(5), 467–470. https://doi.org/10.1130/0091-7613(1995)023<0467:PCAPTM>2.3.CO;2

Veron, J. E. N. (2008). Mass extinctions and ocean acidification: biological constraints on geological dilemmas. *Coral Reefs, 27*(3), 459–472. https://doi.org/10.1007/s00338-008-0381-8

White, R. V. R., & Saunders, A. D. A. (2005). Volcanism, impact and mass extinctions: Incredible or credible coincidences? *Lithos, 79,* 299–316. https://doi.org/10.1016/j.lithos.2004.09.016

Whiteside, J. H., & Grice, K. (2016). Biomarker records associated with mass extinction events. *Annual Review of Earth and Planetary Sciences, 44,* 581–612. https://doi.org/10.1146/annurev-earth-060115-012501

Xu, H. (2010). Synergistic roles of microorganisms in mineral precipitates associated with deep sea methane seeps. In A. Loy, M. Mandl, & L. L. Barton (Eds.), Geomicrobiology: *Molecular and environmental perspective* (pp. 325–346). Berlin: Springer. https://doi.org/10.1007/978-90-481-9204-5_15

Yamakita, S. (1987). Stratigraphic relationship between Permian and Triassic strata of chert facies in the Chichibu Terrane in eastern Shikoku. *Journal of the Geological Society of Japan, 93,* 145–148 (in Japanese).

Yin, H. F., Tong, J. N., & Mang, K. X. (2005). A review on the Global Stratotype Section and Point of the Permian-Triassic Boundary. *Acta Geologica Sinica-English Edition, 79*(6), 715–728.

Yin, H. F., Xie, S., Luo, G., Algeo, T. J., & Zhang, K. (2012). Two episodes of environmental change at the Permian-Triassic boundary of the GSSP section Meishan. *Earth-Science Reviews, 115*(3), 163–172. https://doi.org/10.1016/j.earscirev.2012.08.006

Zhang, G., Zhang, X., Hu, D., Li, D., Algeo, T. J., Farquhar, J., Henderson, C. M., et al. (2017). Redox chemistry changes in the Panthalassic Ocean linked to the end-Permian mass extinction and delayed Early Triassic biotic recovery. *Proceedings of the National Academy of Sciences (U.S.A.), 114*(8), 1806–1810. https://doi.org/10.1073/pnas.1610931114

Zhang, J., Liang, H., He, X., Yang, Y., & Chen, B. (2011). Sulphur isotopes of framboidal pyrite in the Permian-Triassic boundary clay at Meishan section. *Acta Geologica Sinica English Edition, 85,* 694–701.

Zhang, S.-H., Ernst, R. E., Pei, J.-L., Zhao, Y., Zhou, M.-F., & Hu, G.-H. (2018). A temporal and causal link between ca. 1380 Ma large igneous provinces and black shales: Implications for the Mesoproterozoic time scale and paleoenvironment. *Geology, 46*(11), 963–966. https://doi.org/10.1130/G45210.1